Liu *et al. Chem Synth* 2023;3:44
DOI: 10.20517/cs.2023.28

Chemical Synthesis

Review

Open Access

Check for updates

Energy-efficient anodic reactions for sustainable hydrogen production via water electrolysis

Wenxian Liu[1,2,3,*], Xinxin Niu[3], Jiawei Tang[3], Qian Liu[4], Jun Luo[5], Xijun Liu[1,2,*], Yingtang Zhou[6,*]

[1]State Key Laboratory of Featured Metal Materials and Life-cycle Safety for Composite Structures, MOE Key Laboratory of New Processing Technology for Nonferrous Metals and Materials, School of Resources, Environment and Materials, Guangxi University, Nanning 530004, Guangxi, China.
[2]Guangxi Key Laboratory of Electrochemical Energy Materials, Guangxi University, Nanning 530004, Guangxi, China.
[3]College of Materials Science & Engineering, Zhejiang University of Technology, Hangzhou 310014, Zhejiang, China.
[4]Institute for Advanced Study, Chengdu University, Chengdu 610106, Sichuan, China.
[5]ShenSi Lab, Shenzhen Institute for Advanced Study, University of Electronic Science and Technology of China, Shenzhen 518110, Guangdong, China.
[6]Zhejiang Key Laboratory of Petrochemical Environmental Pollution Control, National Engineering Research Center for Marine Aquaculture, Marine Science and Technology College, Zhejiang Ocean University, Zhoushan 316004, Zhejiang, China.

[*]**Correspondence to:** Prof. Wenxian Liu, Prof. Xijun Liu, State Key Laboratory of Featured Metal Materials and Life-cycle Safety for Composite Structures, School of Resources, Environment and Materials, Daxue East Road No.100, Nanning, Guangxi University, Nanning 530004, Guangxi, China. E-mail: liuwx@zjut.edu.cn; xjliu@tjut.edu.cn; Prof. Yingtang Zhou, Zhejiang Key Laboratory of Petrochemical Environmental Pollution Control, National Engineering Research Center for Marine Aquaculture, Marine Science and Technology College, Haida South Road No.1, Zhejiang Ocean University, Zhoushan 316004, Zhejiang, China. E-mail: zhouyingtang@zjou.edu.cn

How to cite this article: Liu W, Niu X, Tang J, Liu Q, Luo J, Liu X, Zhou Y. Energy-efficient anodic reactions for sustainable hydrogen production via water electrolysis. *Chem Synth* 2023;3:44. https://dx.doi.org/10.20517/cs.2023.28

Received: 8 Jun 2023 **First Decision:** 25 Aug 2023 **Revised:** 11 Sep 2023 **Accepted:** 28 Sep 2023 **Published:** 13 Oct 2023

Academic Editors: Bao-Lian Su, Xiang-Dong Yao **Copy Editor:** Dong-Li Li **Production Editor:** Dong-Li Li

Abstract

Overall water splitting is considered as an effective technique for hydrogen (H_2) production; however, it usually requires large operating voltage mainly due to the high equilibrium potential of the anodic oxygen evolution reaction (OER). Replacing OER with energy-saving anode reactions not only reduces the operating voltage for H_2 production but also generates high-value-added chemicals or purifies wastewater. This review article provides an overview of the fundamental reaction principles of overall water splitting and typical energy-saving alternative anode reactions, including methanol oxidation, hydrazine oxidation, and urea oxidation reactions. Then, the preparation methods, regulation strategies, and composition/structure-performance relations of advanced catalysts for these energy-efficient H_2 generation technologies are discussed. Finally, we propose the underlying challenges and perspectives for this promising field.

Keywords: Water electrolysis, hydrogen, oxygen evolution reaction, anodic reactions, energy-efficient

INTRODUCTION

Hydrogen (H_2) is regarded as a promising alternative to fossil fuels due to its high energy density and pollution-free features[1,2]. Traditional H_2 production methods, such as methanol autothermal reforming, coal gasification, and methanol steam reforming ($CH_3OH + H_2O \rightarrow CO_2 + 3H_2$), usually require high temperature and high pressure[3-6]. Moreover, these technologies are often associated with high CO_2 and/or CO emissions, resulting in unsatisfactory H_2 purity and environmental problems[7-11]. In contrast, water electrolysis powered by wind, solar, and electric energy is a green and sustainable technology for the production of high-purity H_2[12]. Generally, water electrolysis systems consist of an anode where the oxygen evolution reaction (OER) takes place and a cathode where the hydrogen evolution reaction (HER) occurs[7]. The theoretical potential for water electrolysis is 1.23 V [*vs.* reversible hydrogen electrode (RHE)]; however, the actual operating voltage usually exceeds 1.5 V due to the inherently sluggish dynamics of the multi-proton coupled electron transfer process in OER[13-15]. In addition, the O_2 produced in the anodic chamber may lead to the explosive O_2/H_2 mixture with the generated H_2 through the gas crossover[16-18].

Replacing OER with other thermodynamically more favorable anodic oxidation reactions can not only reduce the energy consumption of H_2 production and avoid potential explosion risk but also may purify wastewater or produce high-value-added chemicals simultaneously[19-21]. For instance, coupling of the urea oxidation reaction (UOR) with low thermodynamic potential (0.37 V *vs.* RHE) and HER in electrolyzers can not only greatly reduce the hydrogen-producing overpotential but also provide a feasible strategy to treat urea-containing wastewater[22-24]. Combining methanol oxidation reactions (MOR) with HER enables energy-saving H_2 production while generating value-added products such as formic acid and formate[25-27]. Unfortunately, these reactions generally involve complicated multiple electron transfer processes that suffer from slow kinetics and require high-performance catalysts to reduce the energy barriers.

Noble metal-based catalysts (e.g., Pd, Pt, and Ru) show prominent activity for these reactions; however, their large-scale commercialization is subject to the high cost, scarcity, and insufficient stability[28,29]. Alloying noble metals with other inexpensive active components or loading them onto specific carriers such as porous carbon and oxides has been demonstrated to be effective in reducing the dosage of noble metals and improving activity[30-32]. On the other hand, great efforts have been devoted to the development of high-performance non-noble metal catalysts[33-35]. For instance, MoS_2 nanosheet@CoNi-zeolitic imidazole frameworks, NiSe-carbon nanotubes (NiSe-CNTs), and Mo-doped Co_4N were developed to catalyze MOR[36-38]. Ni-Cu alloy nanotubes, Cu-Ni nitride, and CoP-Co_2P were demonstrated to have superior hydrazine oxidation reaction (HzOR) activity[39-41]. Nevertheless, the performance of the non-precious metal-based catalysts developed to date is still not adequate for practical applications. In addition, the energy-saving anodic oxidation reaction and HER go through different reaction paths, which poses a great challenge to the development of high-performance bifunctional catalysts that can reduce the overall cell voltage for H_2 production[42,43]. Therefore, more work should be done to understand the basic reaction principles and design bifunctional catalysts with high activity and stability to advance this emerging field.

Recently, many excellent review papers have summarized the progress of small molecule conversion-assisted H_2 production[8,24,44,45]. For example, Li *et al.* summarized the progress of engineering principles of Ni-based heterostructured catalysts for urea electrolysis[46]. Qiao[24] and Zhu[45] *et al.* summarized the design of catalysts for specific small molecule conversion coupled H_2 evolution systems. Xu *et al.* focused on small-molecule (such as alcohols, aldehydes, amines, and carbohydrates) selection and catalyst design strategies in their recent review[21]. Nevertheless, the systematic summary of the fundamentals of representative energy-saving anodic reactions, as well as the design principles and structure-performance relations to electrocatalysts for these technologies, has rarely been realized.

In this review, we first summarize the reaction principles of OER and HER in water splitting and typical energy-saving anodic reactions, including MOR, HzOR, and UOR. This may help readers understand the elementary steps of these reactions and the interactions of intermediates with active species, thereby stimulating a deeper understanding of the design principles of high-performance catalysts. Then, the preparation methods, regulation strategies, and composition/structure-performance relations of catalysts for energy-efficient H_2 generation technologies, including methanol oxidation-assisted H_2 production (MOAHP), HzOR-assisted H_2 production (HOAHP), urea oxidation-assisted H_2 production (UOAHP), and other biomass conversion-assisted H_2 production are systematically discussed [Figure 1]. This has rarely been realized in other similar reviews and is instructive for researchers to design and synthesize novel efficient catalysts for energy-saving H_2 production. Lastly, possible challenges and some personal insights in this fascinating field are briefly proposed.

FUNDAMENTALS OF ENERGY-SAVING ANODIC REACTIONS-ASSISTED H_2 PRODUCTION

Two half-reactions, i.e., OER at the anode and HER at the cathode, occur simultaneously in a conventional overall water splitting (OWS) device. In different electrolytes, such as acidic, neutral, and alkaline, OER and HER undergo different reaction pathways.

In acidic electrolytes, H^+ acts as the reactant of HER, and the following reaction occurs (Equation 1).

$$2H^+ + 2e^- \rightarrow H_2 \quad (1)$$

The elementary steps of HER in acidic media are as shown in Figure 2A: First, a proton accepts an electron and adsorbs to the active site (Volmer step). Then, two adsorbed hydrogens combine (Tafel step), or the adsorbed hydrogen takes up an electron and reacts with another proton (Heyrovsky step)[27,47].

OER in acidic electrolytes is shown in Equation (2). The possible elementary steps are displayed in Figure 2B.

$$2H_2O - 4e^- \rightarrow 4H^+ + O_2 \quad (2)$$

HER in neutral or alkaline electrolytes is described in Equation (3). The possible elementary steps are shown in Figure 3A.

$$2H_2O + 2e^- \rightarrow 2OH^- + H_2 \quad (3)$$

OER in neutral or alkaline electrolytes is described in Equation (4). The possible elementary steps are described in Figure 3B.

$$4OH^- - 4e^- \rightarrow 2H_2O + O_2 \quad (4)$$

The equilibrium potential for OER is 1.23 V (*vs.* RHE), and the standard potential for HER is 0 V; thus, the thermodynamic potential for OWS is 1.23 V. According to the above equations, OER involves a complex four-electron transfer process, which is inherently sluggish than HER. Therefore, it can be inferred that OER is the bottleneck of OWS in both thermodynamics and kinetics. Tremendous efforts have been made to reduce the overpotential of OER, including the development of noble metal Ir, Ru-based catalysts, or transition metal (Co, Ni, Fe, Cu, *etc.*)-based alloys, oxides/hydroxides, phosphides, sulfides, and selenides.

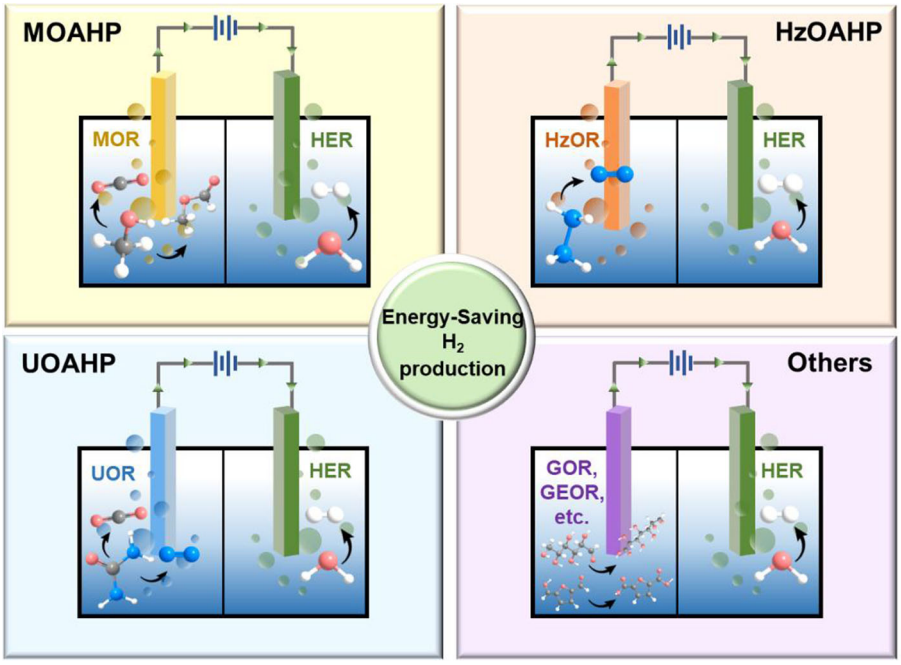

Figure 1. Schematic illustration of the cell configurations for MOAHP, HzOAHP, UOAHP, and other energy-saving anodic reaction-assisted H_2 production. GEOR: Glycerol oxidation reaction; GOR: glucose oxidation reactions; HER: hydrogen evolution reaction; HzOAHP: hydrazine oxidation-assisted H_2 production; HzOR: hydrazine oxidation reaction; MOAHP: methanol oxidation-assisted H_2 production; MOR: methanol oxidation reaction; UOAHP: urea oxidation-assisted H_2 production.

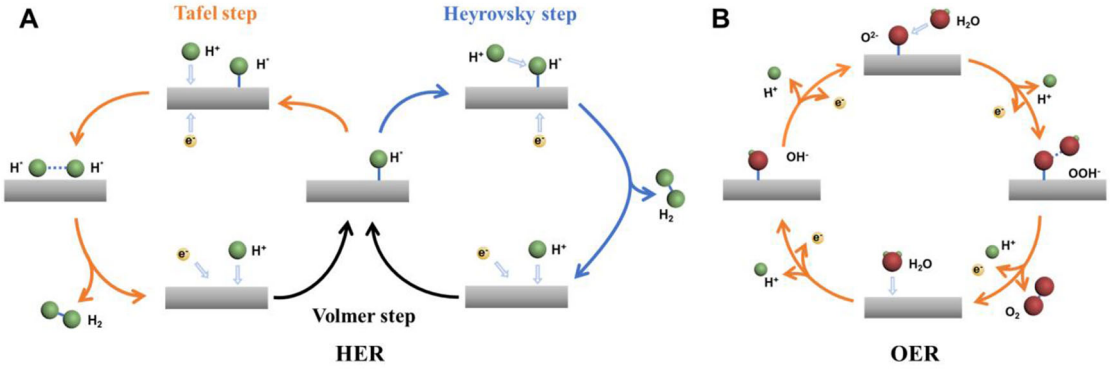

Figure 2. The mechanism for (A) HER and (B) OER in acidic conditions. HER: Hydrogen evolution reaction; OER: oxygen evolution reaction.

In addition, a number of active site regulation strategies, such as the construction of single atomic sites, chemical doping, heterostructuring, and ligand-induced transformation, have been developed to tune the electronic structure of active sites and/or to break the scaling relation of oxygen-containing intermediates (HO_{ads}, O_{ads}, and HOO_{ads}) to accelerate OER processes. Unfortunately, a voltage higher than 1.5 V is still generally required for the actual OER. Alternatively, recent studies have demonstrated that the addition of specific reactants, such as methanol, hydrazine, urea, and glucose, to the electrolyte can effectively reduce the overall potential for H_2 production.

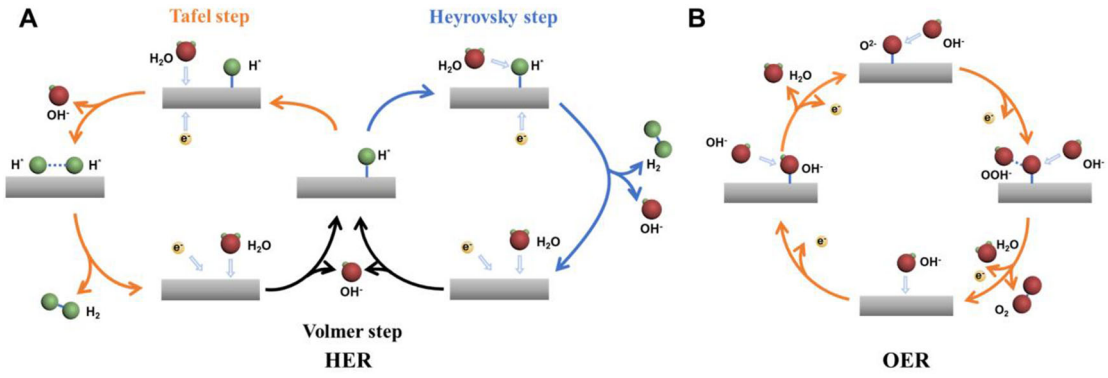

Figure 3. The mechanism for (A) HER and (B) OER in neutral and alkaline medium. HER: Hydrogen evolution reaction; OER: oxygen evolution reaction.

Methanol possesses a much lower oxidation potential than OER. Coupling the MOR with HER was demonstrated to be an effective way for energy-saving H_2 production. Generally, the MOR in alkaline can be described by Equation (5)[48-54]. The main reaction path of methanol oxidation to CO_2 can be divided into a direct pathway [Equation (6)] and an indirect pathway [Equation (7)], depending on the nature of catalysts[55]. For instance, Zeng *et al.* verified that the introduction of Fe and Cu modulates the Pt lattice stress, which will alter the selectivity of direct and indirect pathways for MOR. As a result, the $PtCu_{0.3}Fe_{0.7}$ has a higher CO_2 yield than $PtCu_{0.5}Fe_{0.5}$, and the latter generates more formic acid and methyl formate than the former[56]. Li *et al.* reported a high-entropy alloy composed of $Pt_{18}Ni_{26}Fe_{15}Co_{14}Cu_{27}$ that exhibits excellent MOR and HER activities. This is due to the synergistic effect between multiple active sites optimizing the adsorption energy of key intermediates in the catalytic process [Figure 4A-D]. Moreover, the alloy catalyst shows a high energy barrier for CO formation, resulting in its excellent resistance to methanol poisoning[57].

$$CH_3OH - 6e^- + 6OH^- \rightarrow CO_2 + 5H_2O \quad (5)$$

$$CH_3OH_{ads}\text{-}M \rightarrow CH_2O_{ads}\text{-}M \rightarrow HCOOH_{ads}\text{-}M \rightarrow CO_2 \quad (6)$$

$$CH_3OH_{ads}\text{-}M \rightarrow CH_2O_{ads}\text{-}M \rightarrow CHO_{ads}\text{-}M \rightarrow CO_{ads}\text{-}M \rightarrow CO_2 \quad (7)$$

Hydrazine is another widely used reactant for energy-saving H_2 production because HzOR possesses a low standard potential of -0.33 V (*vs.* RHE) compared to 1.23 V of OER. In addition, electrolyzers coupled with HzOR and HER can avoid the explosion risk of H_2/O_2 in the conventional OER-HER electrolyzer since the product of HzOR is green stable nitrogen (N_2). The equation for the HzOR is described as follows:

$$N_2H_4 - 4e^- + 4OH^- \rightarrow 4H_2O + N_2 \quad (8)$$

The possible elementary steps for the HzOR are shown in Equations (9-12).

$$[N_2H_4]_{ads}\text{-}M - e^- + OH^- \rightarrow H_2O + [N_2H_3]_{ads}\text{-}M \quad (9)$$

$$[N_2H_3]_{ads}\text{-}M - e^- + OH^- \rightarrow H_2O + [N_2H_2]_{ads}\text{-}M \quad (10)$$

$$[N_2H_2]_{ads}\text{-}M - e^- + OH^- \rightarrow H_2O + [N_2H]_{ads}\text{-}M \quad (11)$$

$$[N_2H]_{ads}\text{-}M - e^- + OH^- \rightarrow H_2O + N_2 + M \quad (12)$$

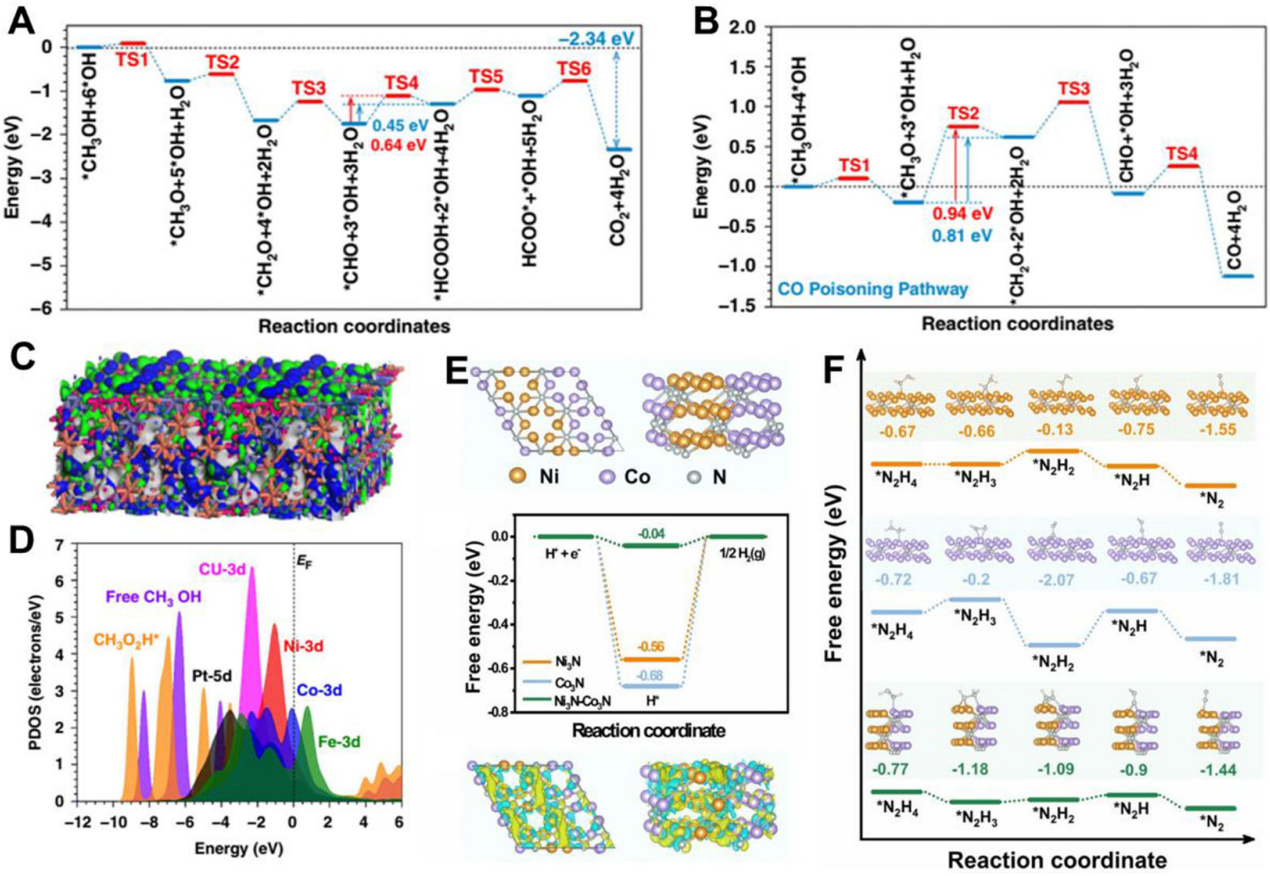

Figure 4. The energetic pathway of (A) MOR and (B) CO poisoning on the surface of $Pt_{18}Ni_{26}Fe_{15}Co_{14}Cu_{27}$; The (C) bonding structure and (D) PDOS of the $Pt_{18}Ni_{26}Fe_{15}Co_{14}Cu_{27}$ [57]; The free-energy profiles for (E) HER and (F) HzOR on Ni_3N-Co_3N and the contrast samples[58]. HER: Hydrogen evolution reaction; HzOR: hydrazine oxidation reaction; MOR: methanol oxidation reaction; PDOS: projected density of state.

The density functional theory (DFT) calculation results of Qian *et al.* in Figure 4E and F confirm that the rate-determining step of HzOR on the (001) surface of Ni_3N is $[N_2H_3]_{ads}$-M → $[N_2H_2]_{ads}$-M with free energy difference of 0.53 eV, while that on the (001) surface of Co_3N is the $[N_2H_2]_{ads}$-M → $[N_2H]_{ads}$-M process with free energy difference of 1.40 eV[58]. After coupling Ni_3N and Co_3N, the rate-determining step is still the deprotonation of $[N_2H_2]_{ads}$-M, but the free energy difference is reduced to 0.19 eV. As a result, Ni_3N-Co_3N heterostructures show better HzOR performance than Ni_3N and Co_3N. In addition, the Ni_3N-Co_3N also exhibits excellent HER activity, allowing a two-electrode HzOR-HER electrolyzer with a low cell voltage of 0.76 V at 400 mA·cm^{-2}. Recently, numerous HzOR catalysts have been developed, such as Ru-doped FeP_4, CuPt and CuPd nanoalloy, and single atom Ru on WS_2[59-62]. However, more efforts need to be made to improve HER/HzOR bifunctional catalytic performance with an in-depth understanding of catalyst design principles and active site regulation strategies.

Urea is a common raw material in industrial wastewater and domestic sewage. A low equilibrium potential of 0.37 V makes UOR another potential alternative to OER for energy-saving H_2 production. Moreover, the UOR-HER electrolyzer provides a potential solution for the purification of urea-containing wastewater during H_2 production. In general, the oxidation products of urea in alkaline electrolytes are CO_2, H_2O, and N_2, and the reaction equation is described as follows.

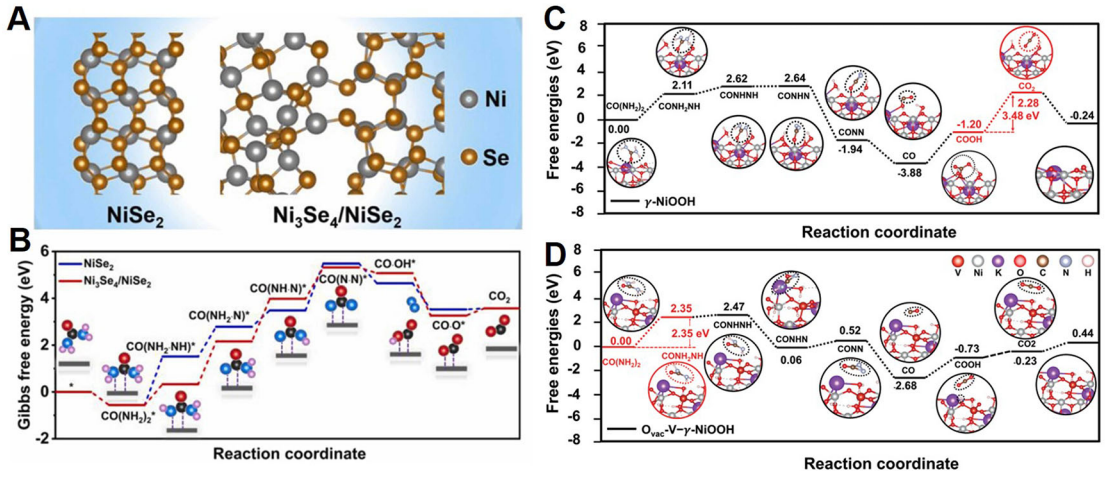

Figure 5. (A) Structure diagram and (B) Gibbs free energy profiles of UOR on $NiSe_2$ and $NiSe_2$-Ni_3Se_4 [65]; Gibbs free energy profiles of UOR on the surface of (C) Ni oxyhydroxide and (D) V-dopant and O-vacancy contained Ni oxyhydroxide[66]. UOR: Urea oxidation reaction.

$$CO(NH_2)_2 - 6e^- + 6OH^- \rightarrow 5H_2O + N_2 + CO_2 \quad (13)$$

According to the deprotonation order of urea, UOR can be divided into the following two typical reaction mechanisms [Equations (14-15)][63,64].

$$[CO(NH_2{\cdot}NH_2)]_{ads}\text{-M} \rightarrow [CO(NH_2{\cdot}NH)]_{ads}\text{-M} \rightarrow [CO(NH_2{\cdot}N)]_{ads}\text{-M} \rightarrow [CO(NH{\cdot}N)]_{ads}\text{-M} \rightarrow [CO(NN)ads\text{-M} \rightarrow CO_2 + H_2O + N_2 + M \quad (14)$$

$$[CO(NH_2{\cdot}NH_2)]_{ads}\text{-M} \rightarrow [CO(NH_2{\cdot}NH)]_{ads}\text{-M} \rightarrow [CO(NH{\cdot}NH)]_{ads}\text{-M} \rightarrow [CO(NH{\cdot}N)]_{ads}\text{-M} \rightarrow [CO(NN)ads\text{-M} \rightarrow CO_2 + H_2O + N_2 + M \quad (15)$$

In these two reaction mechanisms, the UOR both undergoes a complex 6-electron transfer process, which requires rationally designed catalysts to reduce the energetics of the reaction. Precious metals, such as Ru and Ir, and non-precious metal catalysts, such as Ni, Co, and Fe-based catalysts, were demonstrated to have satisfactory UOR performance. Moreover, recent experimental and theoretical studies have demonstrated that the UOR pathway can be regulated by the coordination environment and/or geometric structure of the active sites. Xu *et al.* demonstrated that the UOR on $NiSe_2$ followed Equation (14), with the dehydrogenation of $[CO(NH_2{\cdot}NH)]_{ads}$ to $[CO(NH_2{\cdot}N)]_{ads}$ as the rate-determining step[65]. After coupling $NiSe_2$ with Ni_3Se_4, the rate-determining step becomes $[CO(NH_2{\cdot}NH_2)]_{ads} \rightarrow [CO(NH_2{\cdot}NH)]_{ads}$ with lower reaction free energy [Figure 5A and B]. In another example, UOR follows the mechanism in Equation (15) on the Ni-oxyhydroxide surface, with $[COOH]_{ads} \rightarrow [CO_2]_{ads}$ as the rate-determining step [Figure 5C and D][66]. In addition, Qin *et al.* demonstrated that the introduction of V-dopant and O-vacancy can effectively improve the UOR performance of Ni oxyhydroxide, which delivers a current density of 100 $mA{\cdot}cm^{-2}$ at 1.47 V. In contrast, the pristine Ni oxyhydroxide required a high voltage of 1.60 V to achieve this current density[66].

Although the energy-efficient anodic reactions discussed above, such as glucose oxidation reactions (GOR) and UOR, have low equilibrium potentials, they involve complex multi-electron transfer processes and multiple reaction intermediates. Due to inherent scaling relationships, the energetics of the O- or

N-containing intermediates in anodic oxidation reactions and H* in cathodic HER are difficult to optimize at the active site in a single component and/or coordination environment. Therefore, significant efforts are needed to design and synthesize high-performance bifunctional (e.g., GOR-HER, HzOR-HER, and UOR-HER) electrocatalysts with dual/multiple active centers or specific coordination geometries.

ADVANCED ELECTROCATALYSTS FOR ENERGY-SAVING H_2 PRODUCTION SYSTEMS

Electrocatalysts for MOAHP

Among kinds of small molecule oxidations, MOR has attracted huge attention because of its ultra-low oxidation potential of 0.016 V *vs.* RHE. Due to the advantages of methanol, including its low cost and ease of storage and transfer, MOR is used in fuel cells[67,68]. Impressed, using MOR instead of OER, which has an oxidation potential of 1.23 V, is an economical idea to achieve low energy consumption while efficiently obtaining hydrogen energy. Noble metal-based catalysts are highly active for MOAHP[69]. Over the decades, a great deal of design strategies for noble metal catalysts have been proposed. Zhang *et al.* employed a selective Pt nanoplate as an active site to create a catalyst to achieve MOAHP[70]. They prepare vertical graphene nanosheet arrays with Pt nanoplates decorated grown on the carbon cloth (Pt200-VGNSAs/CC). Benefited from the three-dimensional (3D) structure, large surface area, and conductivity from arrays, they achieved high mass activity of 1,050 $mA \cdot mg^{-1}$, 0.38 V *vs.* Ag/AgCl for MOR, and overpotential of 60 mV @ 10 $mA \cdot cm^{-2}$ for HER. Similarly, Feng *et al.* choose $PtTe_x$ as a template to prepare a new class of Pt superstructures (SSs) via electrochemical leaching of Te[71]. Different distorted degrees among H-/M-/W-Pt SSs/C were caused by differences in Te content. The distorted surface in materials can effectively mitigate the detrimental influence of agglomeration/degradation. Thus, H-Pt SSs/C showed a mass activity of 2.24 $A \cdot mg^{-1}$ at 0.9 V for MOR and a 25.3 mV overpotential to arrive at 10 $mA \cdot cm^{-2}$ for HER. As shown in Figure 6A, molecular dynamics (MD) and DFT calculations revealed that excellent performance results from the synergistic effects of surface compression, surface defects, and nanopores in the catalytic process.

Although noble metals show good performance of MOAHP, adding a second composite can not only optimize the stability of catalysts but also decrease the cost of noble metals. Thus, Ma *et al.* attained a Pt-NP/NiO-NS catalyst by depositing Pt nanoparticles onto the ultrathin NiO nanosheets via the cyanogel-$NaBH_4$ method[72]. The material showed satisfied catalysis performance with 179.9 $mA \cdot cm^{-2}$ at 1.45 V for MOR and an overpotential of 57 mV @ 10 $mA \cdot cm^{-2}$ for HER. The MOAHP device based on Pt-NP/NiO-NS could achieve product hydrogen and potassium formate at 1.39 V. The high activity of the material was due to the synergistic effect between the two composites; in addition, Pt-NP could enhance the activity of $Ni^{III}OOH$ species, which accelerated HER processes [Figure 6B]. Li *et al.* chose to modify the Pt-based catalyst by phosphating, and they constructed a heterogeneous structure catalyst of porous Pt/Pt_5P_2 nanocages[73]. Theoretical calculations revealed the mechanism of the phosphating strategy. As shown in the inset of Figure 6C, Pt/Pt_5P_2 clearly exhibited an electron-rich area around P atoms. For HER, the introduction of P atoms changed the electron configuration of Pt, optimizing the adsorption strength of intermediate H*. Figure 6C shows the HzOR process of Pt/Pt_5P_2; the energy barrier from *CHO to *HCOOH was also decreased. Pt/Pt_5P_2 exhibited a mass activity of 1.37 $A \cdot mg^{-1}_{Pt}$ for MOR and 29 mV overpotential @10 $mA \cdot cm^{-2}$ for HER. Modification of precious metals by alloy materials is also an effective strategy. Guo *et al.* chose a metal doping strategy, used Co nanosheets as bridges, and prepared Co-doped Rh nanoparticle catalysts on carbon black (Co-Rh_2)[74]. The energy barrier of converting *CO into COOH* during MOR processes was decreased by a Co-doping strategy. As a result, the catalyst showed high mass activity of 889 $mA \cdot mg^{-1}$ and just 2 mV overpotential for HER. As displayed in Figure 6D, the MOAPH device constructed by Co-Rh_2 can reach 10 $mA \cdot cm^{-2}$ at 1.545 V.

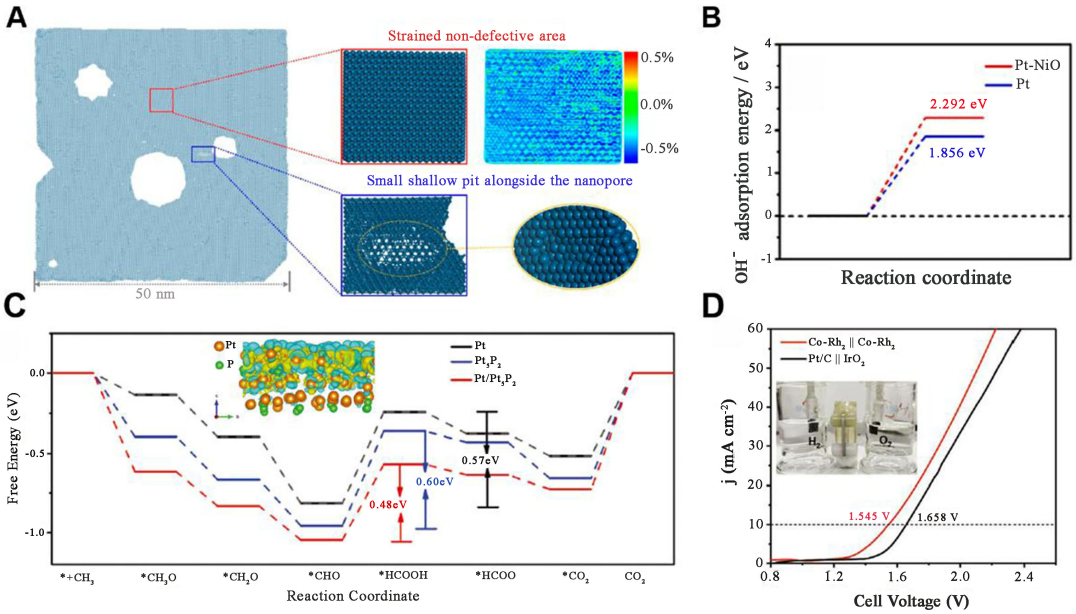

Figure 6. (A) MD calculation of H-Pt SSs/C. The right side is the atomic structure after 2,000 ps, the top is the area of nondetective and strained regions, and the bottom is the area of single atom layer nanopits[71]; (B) DFT calculation of OH^- absorption energy for NiO after Pt introduction[72]; (C) Calculated results of energy for MOR processes of Pt, Pt_5P_2, and Pt/Pt_5P_2[73]; (D) LSV curve of the Co-Rh_2-based MOAHP device, the inset is an optical image of the device[74]. DFT: Density functional theory; LSV: linear sweep voltammetry; MD: molecular dynamics; MOAHP: methanol oxidation-assisted h_2 production; MOR: methanol oxidation reaction; SSs: superstructures.

Noble metal catalysts have very significant electrochemical performance, but their practical applications are often limited by their high cost and complex preparation technology[29]. Forming an alloy of noble metals with other affordable metals can reduce the containing of noble metals, which helps reduce the cost. Meanwhile, the alloying strategy decreases the possibility of poisoning, leading to deactivation by changing the electronic structure. Considering this, Ren *et al.* constructed PtCo alloy nanoparticles and encapsulated them with N-doped nanorod arrays (Pt_2Co_8@NC)[75]. High specific surface area and abundant active sites endow the Pt_2Co_8@NC with good activity. The MOR catalytic performance included a forward anodic peak current density of 2.17 mA·cm^{-2}, a retention rate of 94.4% after 100 cycles, and an overpotential of 12 mV for HER @10 mA·cm^{-2}. Jiang *et al.* prepared core-shell structure Pd@RhPd nanodendrites (NDs) by galvanic replacement reacting Pd NDs and rhodium trichloride[76]. They found that the content of Rh in Pd@RhPd NDs determined the MOR catalytic activity. While the introduced Rh could improve the HER activity of the material, its content had little effect on HER activity. The Pd@$Rh_{0.07}$Pd ND-based MOAHP device can achieve a current density of 10 mA·cm^{-2} at 0.813V. Yin *et al.* synthesized a highly active catalyst for crimp-perforated PdLn bimetallene with abundant defects via a solvothermal method[77]. The crimp-perforated structures endow PdLn bimetallene with high surface energy and expanded active sites. The constructed MOAHP device with PdLn bimetallene could achieve a current density of 100 mA·cm^{-2} at a low voltage of 1.26 V. In addition, as a special alloy species, high-entropy alloys have been widely used in the preparation of various catalysts and are also used in MOAHP devices. Wang *et al.* constructed a rambutan-like Au@PdRu catalyst with a core-shell structure[78]. The unique structure provided more exposed active sites for the material. Therefore, Au@PdRu displayed the mass activity of 1.56 A·mg$^{-1}_{Pd}$ for MOR, and MOAHP devices of 0.88 V reached 10 mA·cm^{-2}, while for OWS, it was 1.69 V. Differently, Sarno *et al.* using non-noble metal components to prepare the catalysts. They first proposed using MoS_2-modified PtRh alloy through a wet chemical method[79]. The modified PtRh/MoS_2 showed better stability than the unmodified one, with no obvious decay observed after 2,000/600 cycles for HER/MOR. They used the I_f/I_b ratio (I_f is

forward peak current density, and I_b is backward peak current density) to quantify the poison tolerance of the catalyst, which was 2.37 V for PtRh/MoS_2. This great performance could be attributed to the abundant edges of MoS_2 nanosheets, providing an additional surface for stabilizing PtRh.

Lu *et al*. prepared a sea urchin-like heterogeneous material encapsulating $CoPt_3$@Co_2P with Co embedded in N_2-doped carbon nanotubes ($CoPt_3$@Co_2P/Co@NCNT)[80]. The DFT calculation told the original of the catalytic performance improvement, electrons transferred from $CoPt_3$ to Co_2P assisting by the heterogeneous interfaces. This process would generate the electron hole region in $CoPt_3$, which benefited MOR processes, and the electron-rich Co_2P would optimize H* absorption energy of HER processes. Thus, $CoPt_3$@Co_2P/Co@NCNT exhibited MOR catalytic activity of 2,981 mA·mg^{-1}_{Pt} and HER overpotential of 19 mV @10 mA·cm^{-2}, and MOAHP could arrive at 10 mA·cm^{-2} at 1.43 V.

In addition to noble metal catalysts, non-noble metal catalysts with good stability and low cost have also received attention in recent years. Many studies have demonstrated that non-noble metal catalysts can exhibit comparable activity to noble metal catalysts through rational structural/component designs. As shown above, MoS_2 nanosheets have an abundant edge structure, which is conducive to catalysis. Thus, Liu *et al*. constructed CoNi-ZIF composites embedded with MoS_2 nanosheets [MoS_2@CoNi-ZIF (3-1)][37]. The MoS_2@CoNi-ZIF (3-1) showed a mass activity of 430.08 mA·g^{-1} for MOR and could work stable for 3,000 s. The HER performance achieved an overpotential of 80 mV to reach 10 mA·cm^{-2} and maintained 97.5% after a 48-h cycle. In addition to MoS_2, Peng *et al*. selected $MoSe_2$ and NiSe to form a hetero-structured NiSe/$MoSe_2$ grown on carbon cloth (NMS/CC, Figure 7A)[81]. The catalyst could achieve 100 mA·cm^{-2} at 1.38 V for MOR, and the Tafel slope of OER was ~ 14 times that of MOR. At the same time, NMS/CC could cycle stably for 120 h, as measured by the *I-t* test for MOR. Impressed, the NMS/CC-based MOAHP device could be powered by a 1.5 V solar battery.

Zhao *et al*. also selected NiSe as the active material and prepared the highly dispersed hollow h-NiSe/CNTs/CC heterogeneous catalyst via the one-pot method[36]. Interestingly, they chose the methanol oxidation route that produces formate, a high-value product, rather than conventional CO_2. In detail, benefiting from the 3D CNT network and highly dispersed NiSe crystals, the MOAHP device constructed by h-NiSe/CNTs/CC could arrive 345 mA·cm^{-2} current density, high Faraday efficiency of 95% @1.62V, and nice stability, which can improve the H_2 production efficiency ~ six times [Figure 7B]. Subsequently, they further studied the mechanism of h-NiSe/CNTs by DFT calculation. The results showed that the SeO_x and NiOOH produced during the catalytic process can optimize the d-band center to achieve the selective oxidation of methanol and avoid further oxidation to CO_2 [Figure 7C]. Choosing the MOR route without CO_2/CO production or any gas production not only ensures the purity of H_2 produced but also achieves higher economic benefits through the formation of formate/formate salts[82-85]. Therefore, Du *et al*. also opted for the CO-free MOR route but chose to use formate as a product by designing a $NiFe_2O_4$ catalyst ($NiFe_2O_4$/NF) and using alkaline seawater as electrolyte[86]. The $NiFe_2O_4$/NF achieved a current density of > 800 mA·cm^{-2} and a high Faraday efficiency (96% for HER and 95% for MOR) in alkaline seawater. Impressively, the material showed great chlorine corrosion resistance and could cycle stably for more than 6 h at a large current density of 700 mA·cm^{-2}. Importantly, as shown in Figure 7D, utilizing MOR instead of OER actually avoids the chlorine evolution reaction (ClER).

Electrocatalysts for HOAHP

HzOR shows a small overpotential of -0.33 V *vs*. RHE. The H_2 production device constructed by the combination of HzOR and HER can achieve the purpose of low consumption and high economic value[87]. Jia *et al*. designed N-doped nanobowls (Rh/N-CBs) grown with ultrafine Rh nanoparticles[88]. When the Rh/

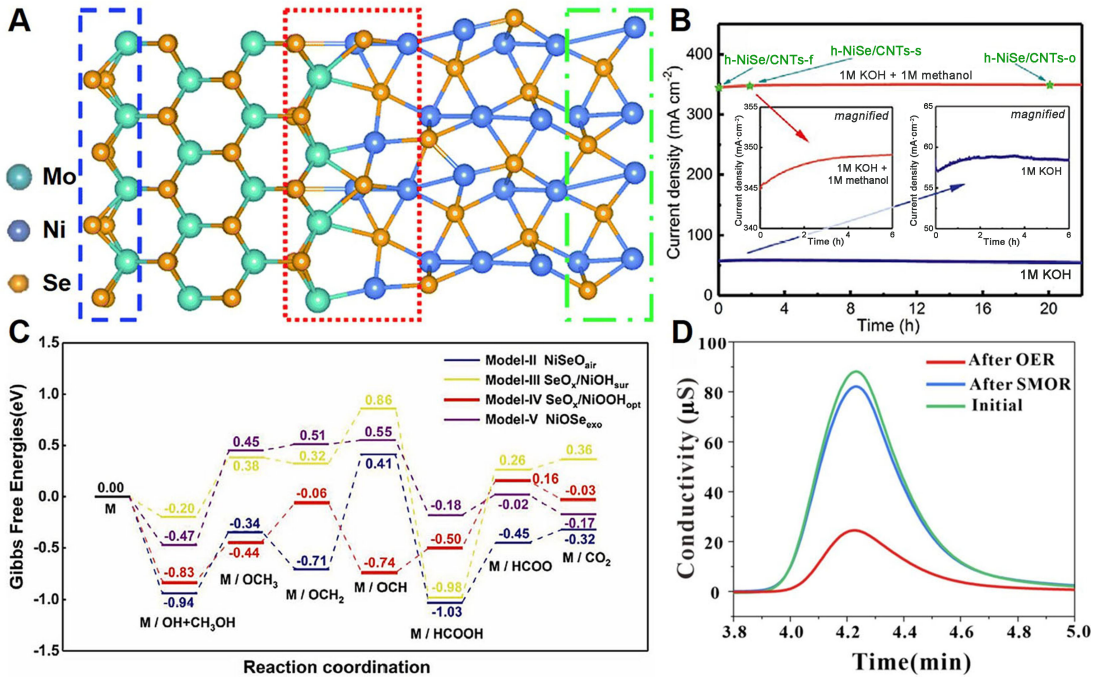

Figure 7. (A) Simulated heterogeneous interface in NMS/CC[81]; (B) Stability of h-NiSe/CNTs/CC at 1.62 V[36]; (C) DFT calculation of h-NiSe/CNTs/CC during HzOR process[36]; (D) Ion chromatograms of Cl^- for initial seawater, after SMOAHP and SOWS with catalysts of $NiFe_2O_4$/NF[86]. CC: Carbon cloth; CNTs: carbon nanotubes; DFT: density functional theory; HzOR: hydrazine oxidation reaction; NMS: NiSe/$MoSe_2$; NF: $NiFe_2O_4$; SMOAHP: methanol oxidation-assisted H_2 production in seawater; SOWS: overall water splitting in seawater.

N-CBs were used for HOAHP devices, a current density of 20 mA·cm^{-2} at a low cell voltage of 0.2 V was achieved. DFT calculations revealed that the bonding between pyrrole-N and Rh in N-CBs resulted in near-zero adsorption energy of hydrogen, which endowed the Rh/N-CBs with good catalytic performance [Figure 8A]. Thus, when N-doped, the Rh site will strongly bond with N, which can tune the electron structure. Zhang *et al.* reported the preparation of Rh_2S_3 with N-doped carbon catalysts and applied Rh_2S_3/NC to HOAHP devices in a wide pH range[89]. As shown in Figure 8B, the DFT calculation demonstrated that the great performance not only came from N-doping but also from the longer N-N bonds on the Rh_2S_3 surface. Compared to Pt, during HzOR, adjacent S atoms can provide abundant charges to stabilize the Rh site, leading to an improvement in electrocatalysis performance. Therefore, Rh_2S_3/NC had lower energy of H adsorption and NHNH adsorption dehydrogenation. Benefited from these, Rh_2S_3/NC showed low HER overpotentials of 38, 46, and 21 mV in alkaline, neutral, and acidic electrolytes (@10 mA·cm^{-2}) and saving energy consumptions of 93.3%, 85.2%, and 78.3% compared to OWS, respectively. Yang *et al.* designed a Ru nanocluster-modified mesoporous nanosphere (Ru_{20}@mONC) and applied it to a wide pH range HAOHP device[90]. Ru_{20}@mONC demonstrated better electrocatalysis performance, achieving current densities of 10/100 mA·cm^{-2} at 39/429, 164/1,141, and 405/926 mV for alkaline, neutral, and acidic conditions, respectively. It also exhibited stable cycling for 40/20/40 h.

The alloying strategy was also useful for HzOAHP catalysts design. Yu *et al.* prepared a Au_1Pt_8 alloy via pulsed laser irradiation and sonochemical processes [Figure 8C][91]. During testing, Au_1Pt_8 showed excellent HER performance, achieving a 26 mV overpotential to reach 10 mA·cm^{-2} in alkaline electrolytes and 502 mV for HzOR. Compared to OWS, Au_1Pt_8-derived HOAHP devices can arrive at 10 mA·cm^{-2} at just 0.172 V and work stable over 10 h. DFT calculations showed the mechanism of Au_1Pt_8 that a long pair of nitrogen in N_2H_4 will bind with empty orbitals of Pt in the alloy, optimizing the HzOR electrocatalysis

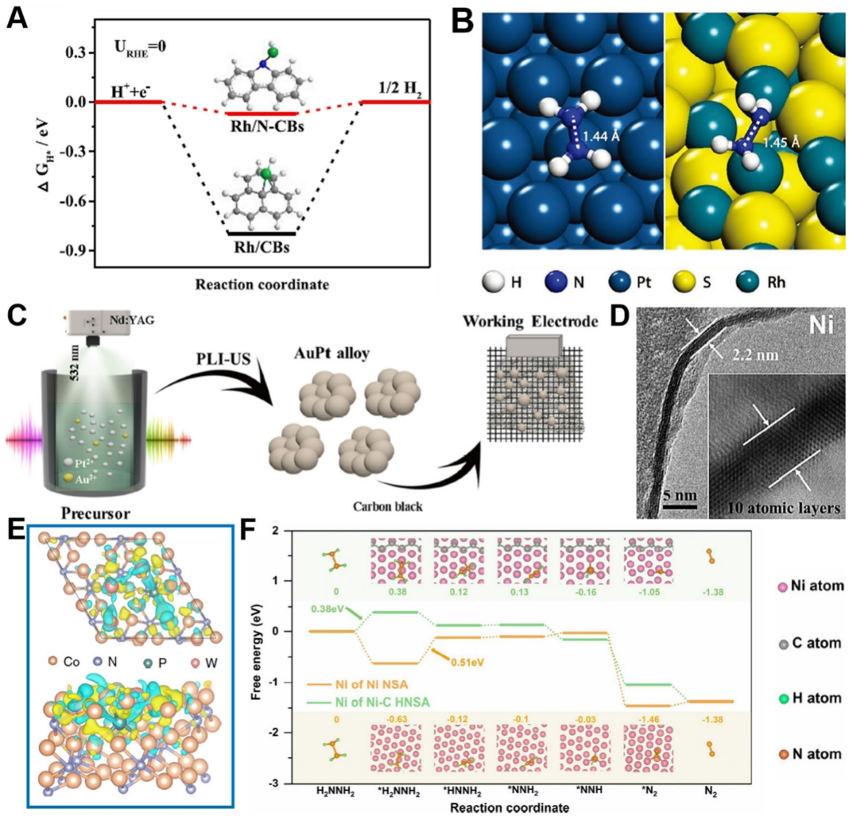

Figure 8. (A) Adsorption energy of hydrogen for Rh/N-CBs and Rh/CBs[88]; (B) Schematic diagram of N_2H_4* adsorption mode on Pt and Rh_2S_3 surfaces[89]; (C) Synthesis scheme of Au_1Pt_8 alloy[91]; (D) TEM images of $Ni(OH)_2$ layers and Ni nanosheets (inset)[92]; (E) The charge density difference of P, W-Co_3N NWA/NF. Top-view (top) and side-view (bottom), cyan/yellow demonstrate charge depletion/accumulation[93]; (F) The calculation of Ni NSA and Ni-C HNSA of HzOR processes[95]. HNSA: Hybrid nanosheets; HzOR: hydrazine oxidation reaction; N-CBs: nitrogen-doped carbon nanobowls; NF: $NiFe_2O_4$; NSA: nanoarrays; NWA: nanowire array; TEM: transmission electron microscopy.

performance. They also constructed CuPd alloy (Cu_1Pd_3/C) via pulsed laser ablation (PLA)[61]. Cu_1Pd_3/C showed an overpotential of 0.505 V to reach 10 mA for HOAHP devices; thus, this performance can be attributed to the introduction of Cu. Cu will synergize with Pd to form a solid colloidal solution, adjusting the electron structure of materials and improving the adsorption capacity of the reaction intermediate. Ge *et al.* prepared PtCu nanoalloys (PtCu-NA) by utilizing Cu_2O as a template[60]. Thanks to the synergistic effect between Cu and Pt, the PtCu-NA exhibited HER and HzOR overpotentials of 224 and 668 mV @10 mA·cm^{-2}, respectively. PtCu-NA-based HOAHP devices required only 0.666 V to achieve 200 mA·cm^{-2} and could stably cycle over 110 h without obvious decay.

Non-noble metal-based catalysts also showed great performance in HzAOHP catalysts. Kuang *et al.* prepared ultra-thin Ni nanoarrays (Ni-NSA) through *in-situ* topological reduction of $Ni(OH)_2$ nanosheets and superhydrophobic arrangement as the carrier[92]. When applied in HzOR, it showed specific activity (227.6 mA·cm^{-2}) and high mass activity (406.4 mA·mg$^{-1}_{cata}$) at 0.25 V, which is 1.81 and 3.25 times higher than that of Pt/C. As shown in Figure 8D, the great performance can be attributed to the ultra-thin nature of Ni-NSA, which consists of just ten atomic layers. As in many previous studies, transition metal nitrides (TMNs) exhibit excellent electrical conductivity, low resistance, and excellent stability in acid/base environments and are commonly used as catalysts. Therefore, Wang *et al.* designed a double-component TMN heterostructure catalyst Cu_1Ni_2-N[40]. The structure of TMNs and 3D structures of the carrier [carbon

fiber cloth (CFC)] gave Cu_1Ni_2-N good catalytic performance. It showed a 71.4 mV overpotential for HER and 0.5 mV for HzOR at 10 mA·cm^{-2}. The HOAHP device constructed by Cu_1Ni_2-N not only achieved 10 mA·cm^{-2} at 0.24 V but also had good stability for 75 h. Liu *et al.* chose Co_3N as TMNs to design catalysts with P, W co-doping (P, W-Co_3N NWA/NF)[93]. Among the catalysts, P, W co-doping optimized the electron structure of Co_3N, which decreased the free energy of dehydrogenation *NHNH to form *N_2H during the key step of the process [Figure 8E]. Meanwhile, hydrogen adsorption energy was obviously reduced, which was influenced by the decrease of the d-bond center in Co_3N. Therefore, P, W-Co_3N NWA/NF exhibited HzOR catalytic activity of -55 mV, HER catalytic activity of -41 mV, and an impressive HOAHP device potential of 28 mV (all @10 mA·cm^{-2}). In addition to TMNs, there are also many other active materials. Tang *et al.* prepared hollow $CoSe_2$/$MoSe_2$ nanospheres with a "reinforced concrete structure"[94]. Benefiting from the tightly bound interface between $CoSe_2$ and $MoSe_2$, the material arrived 10 mA·cm^{-2} at 168 mV for HER and 386 mV for HOAHP devices. Zhu *et al.* constructed a double active site catalyst on Ni/C hybrid nanosheets (Ni-C HNSA) [95]. In detail, one of the active sites was the exposed surface of Ni particles for HzOR, as it exhibited favorable N_2H_4 dehydrogenation kinetics [Figure 8F]. The other active site was a core-shell Ni@C for HER, as the carbon site could show a thermal-neutral H* adsorption value of 0.1 eV. Therefore, Ni-C HNSA displayed good catalytic activity, and the HOAHP device constructed by it only required 0.14 V to achieve 50 mA·cm^{-2}.

In order to maximize the utilization of resources, many electrolytic hydrogen energy devices chose seawater as the electrolyte[96-98]. However, for traditional OWS, the OER potential approaches the ClER potential (1.71 V *vs.* RHE), which may lead to the formation of harmful gas[85,99]. Instead, HOAHP systems in seawater can effectively avoid the ClER. Deng *et al.* prepared a defect-rich low-crystalline Rh metallene (*l*-Rh metallene) hetero-phase structure catalyst applied for HOAHP in seawater[100]. The low-crystalline structure can easily be observed from the TEM image in Figure 9A. The hetero-phase structure enables *l*-Rh metallene to have large surface area and more exposed active sites. When used as an electrocatalyst, it showed a -38 mV overpotential for HER and -2 mV overpotential for HzOR (both at 10 mA·cm^{-2}), and *l*-Rh metallene-based HOAHP systems in seawater achieved a current density of 10 mA·cm^{-2} at only 28 mV. Modification of noble metal components can not only optimize catalytic performance but also reduce the cost, contributing to the development of HOAHP devices. Therefore, Zhai *et al.* prepared MIL-(IrNiFe)@NF catalysts by *in-situ* growing micro-spherical-shaped Ir-doped NiFe arrays[101]. The unique hierarchical structure of MIL-(IrNiFe)@NF enabled it to achieve 1,000 mA·cm^{-2} in traditional seawater electrolysis at 1.9 V and only 0.69 V in HOAHP devices while maintaining stable cycling for 24 h [Figure 9B]. They also prepared Ru-FeP_4 nanosheets on Fe foam (IF) via *in-situ* grown methods. The HOAHP derived from Ru-FeP_4/IF needed 0.9 V to achieve the same 1000 mA·cm^{-2} in seawater[59]. Subsequently, through DFT calculations [Figure 9C], they further explored the catalyst mechanism of Ru-FeP_4/IF. They found that Ru doping could adjust the electronic structure, which optimized the adsorption energy of H* and accelerated the dihydrogen process of *N_2H_4. For non-noble metal-based HOAHP catalysts, Wang *et al.* prepared Fe-doped Ni_2P/CoP, which was encapsulated by ultra-thin N-doped carbon layers (Fe-CoNiP@NC)[102]. When applied as catalysts in HOAHP devices, Fe-CoNiP@NC showed 100% Faradaic efficiency (FE) and long-term stability for 100 h. Specifically, the SHOAHP device based on it could save 4.03 kWh per 1.0 m^3 generated compared to OWS [Figure 9D]. In addition to this, in Figure 9E, Guo *et al.* prepared MoNi alloys and achieved high catalytic performance by using MoO_2 nanorods as carriers[103]. The MoNi@NF-based HOAHP device could achieve 1,000 mA·cm^{-2} at a low voltage of 0.54 V in seawater while also demonstrating cycle stability for 100 h. The good performance of the material could originate from the spatial structure, good interfacial conductivity of MoO_2, and strong synergistic effect between MoO_2 and the MoNi alloys.

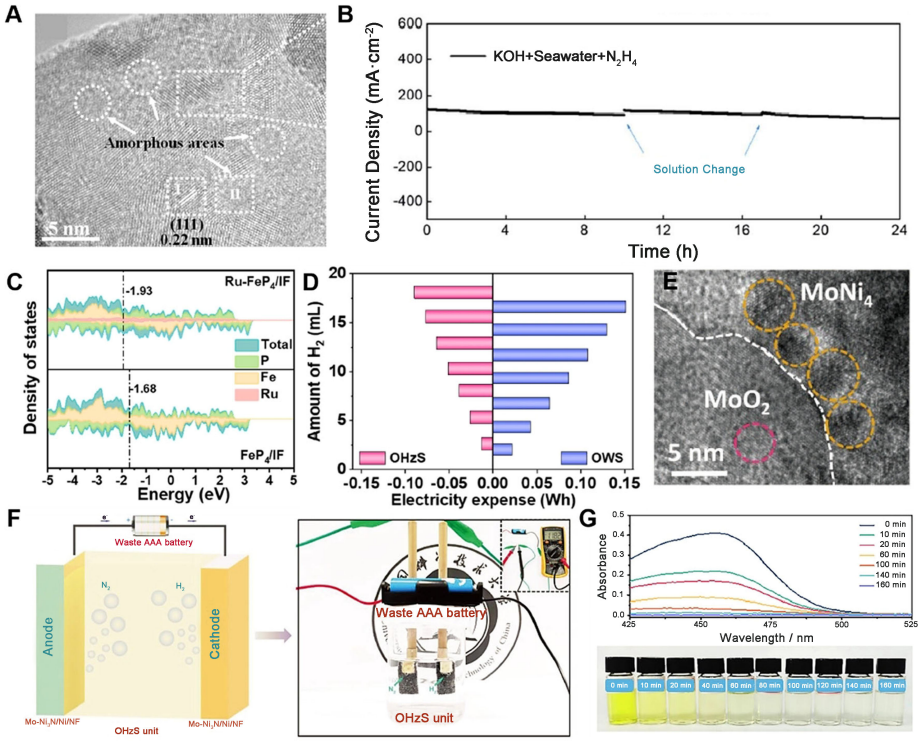

Figure 9. (A) TEM image of *l*-Rh metallene[100]; (B) Cycle stability of MIL-(IrNiFe)@NF-based HOAHP devices at 0.69 V in seawater[101]; (C) The DOS change after Ru-doped of Ru-FeP_4/IF[59]; (D) Electricity expense of Fe-CoNiP@NC-based HOAHP and OWS devices[102]; (E) TEM image of MoNi@NF[103]; (F) The scheme and optical images of Mo-Ni_3N/Ni/NF-based HOAHP with driving by used AAA batteries[104]; (G) Optical images of comparison of wastewater degradation with Fe/F-Ni_2P@NC as catalysts at different times[105]. DOS: Density of states; HOAHP: hydrazine oxidation-assisted H_2 production; l-Rh metallene: low-crystalline Rh metallene; OWS: overall water splitting; TEM: transmission electron microscopy.

In addition to realizing H_2 production from SHOAHP devices without harmful gas generation, MOR has many applications in the reuse of wastewater or used batteries. Liu *et al.* formed heterostructures between Mo-doped Ni_3N and porous nanosheets to obtain Mo-Ni_3N/Ni/NF catalysts, which enabled HOAHP devices to achieve 10 mA·cm^{-2} at 55 mV[104]. Surprisingly, they built an environmentally friendly and green production system of Mo-Ni_3N/Ni/NF by using waste 1.5 V AAA batteries driving the HOAHP device, as shown in Figure 9F. As wastewater containing N_2H_4 is difficult to handle due to its high salinity, Zhang *et al.* prepared Fe/F-Ni_2P@NC catalysts by doping strategies[105]. Fe/F-Ni_2P@NC can not only realize efficient SHOAHP devices but also rapidly degrade ~ 5 ppb when the electrolyte is wastewater with N_2H_4 [Figure 9G].

Electrocatalysts for UOAHP

UOR can convert urea into CO_2 and N_2 with a low theoretical voltage (0.37 V *vs.* RHE). Coupling UOR with HER provides an energy-saving route for H_2 production[45,106-108]. Nowadays, transition metals with low prices and abundant reserves are widely considered[109-112]. Currently, many researchers have adopted a series of different strategies to prepare UOR catalysts with excellent properties. One common strategy is to modify transition metal sites with oxygen, sulfur, phosphorus, and other non-metallic elements[113,114]. For example, Hu *et al.* successfully synthesized a nickel nitride bead nanosphere array (Ni_3N/NF) grown on nickel foam[115], and this material can be used as high-performance bifunctional catalysts for UOR and HER. The current density of the two-electrode cell constructed with this catalyst can reach 100 mA·cm^{-2} at 1.42 V, while the corresponding voltage of the cell constructed with Pt/C and IrO_2 is 1.60 V, indicating that Ni_3N/NF is superior to precious metals.

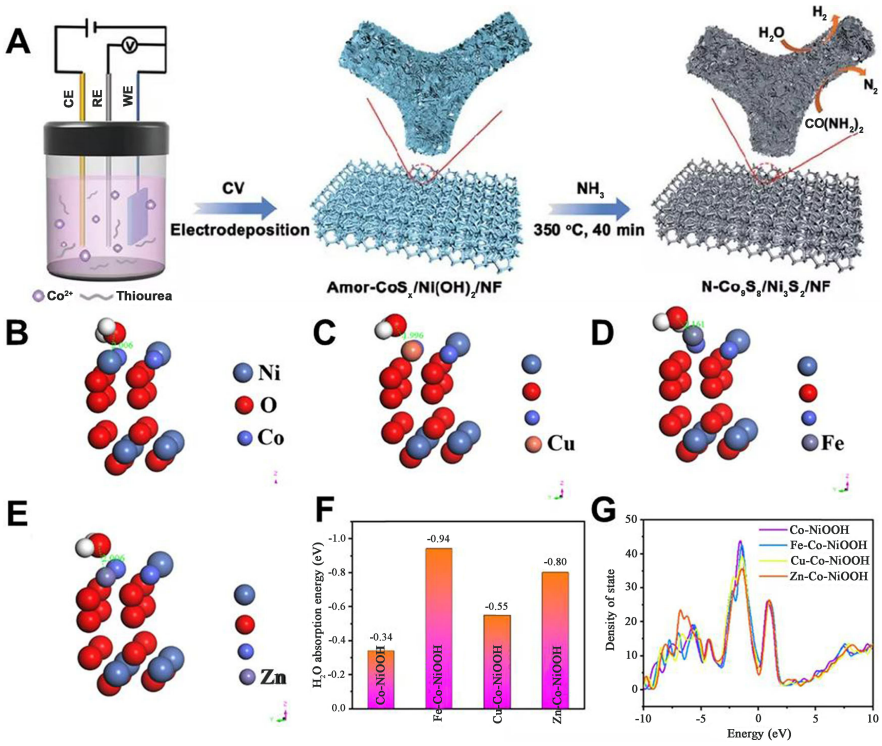

Figure 10. (A) Synthesis path diagram of N-Co_9S_8/Ni_3S_2/NF[122]; The ball-and-bat model of H_2O adsorbed on (B) Co-NiOOH, (C) Cu-Co-NiOOH, (D) Fe-Co-NiOOH, (E) Zn-Co-NiOOH; (F) Adsorption free energy bar diagram of H_2O on Co NiOOH, Fe-Co-NiOOH, Cu-Co-NiOOH, and Zn-Co-NiOOH; (G) Schematic diagram of calculated state density of Co NiOOH, Fe-Co-NiOOH, Cu-Co-NiOOH, and Zn-Co-NiOOH[123].

The combination of two or more kinds of active sites into a multi-component catalyst is another feasible strategy[116,117]. Bimetallic synergies can effectively improve the catalytic activity. For example, Sha *et al.* have *in-situ* grown NiCoP on carbon cloth (NiCoP/CC) in the shape of a prickly leaf[118]. Due to the synergistic effect of Ni and Co and its unique hierarchical structure, the catalyst showed excellent electrocatalytic activity. The urea electrolytic cell assembled with NiCoP/CC as anodes and cathodes at the same time has a voltage of 1.42 V at the current density of 10 mA·cm^{-2}, which is 160 mV lower than that of the electrolytic cell without urea. Wang *et al.* prepared layered coral-like Ni-Mo sulfide (HC-NiMoS/Ti) on Ti grids through a simple hydrothermal and vulcanization process[119]. Due to the unique layered coral-like nanostructure, abundant active sites, fast charge transfer rate, and the synergy between multiple components, the electrocatalytic performance of HC-NiMoS/Ti has been greatly improved. The cell voltage of this catalyst is only 1.59 V when reaching a current density of 10 mA·cm_{-2} in 1.0 M KOH + 0.5 M urea.

In addition, element doping can be used to further improve the catalytic performance of single-component or multi-component catalysts. This strategy can effectively regulate the electron configuration state inside the catalyst, which plays a great role in the improvement of material properties[120,121]. For example, Xie *et al.* synthesized N_2-doped Co_9S_8/Ni_3S_2 hybrid nanosheet arrays (N-Co_9S_8/Ni_3S_2/NF) on nickel foam substrates through electrodeposition combined with ammonification reaction, and the diagram of their synthesis process is shown in Figure 10A[122]. On the one hand, the unique two-dimensional porous nanosheet structure of the catalyst can expose more heterogeneous interfaces between Co_9S_8 and Ni_3S_2 so as to provide abundant reactive sites and accelerate the electron transport rate. On the other hand, the doping of N_2 regulates the internal electronic structure of the catalyst and further enhances its electrocatalytic activity. N-Co_9S_8/Ni_3S_2/NF finally showed excellent HER and UOR performance: The potential of HER at

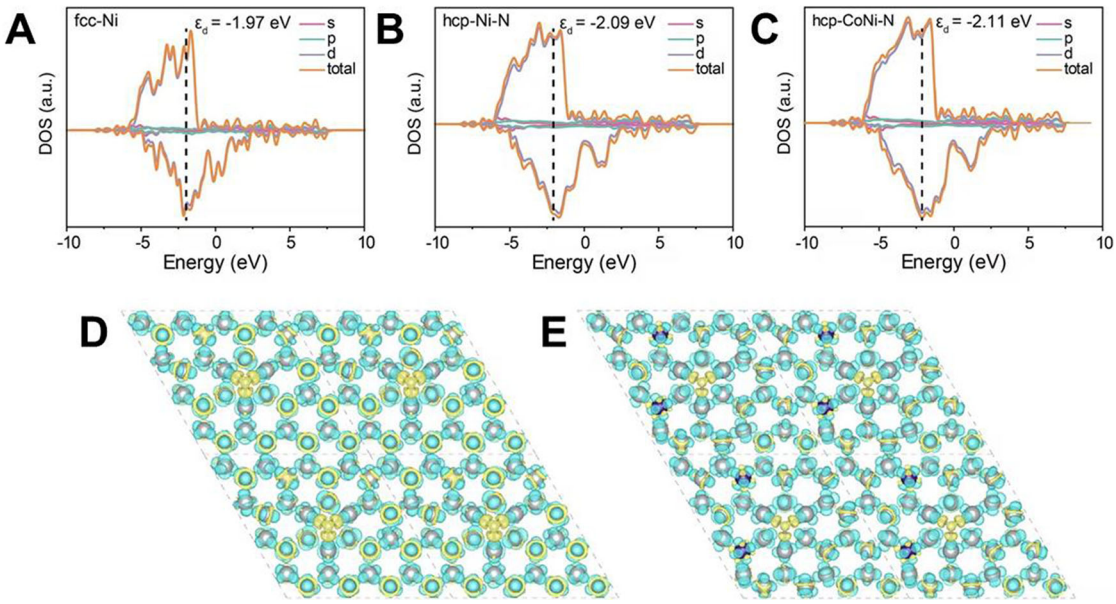

Figure 11. Schematic diagram of calculated state density of (A) fcc-Ni; (B) hcp-Ni-N; and (C) hcp-CoNi-N; Charge density difference analysis model of (D) hcp-Ni-N; and (E) hcp-CoNi-N, where yellow represents electron gain and cyan represents electron loss[124].

10 mA·cm^{-2} was only 111 mV, while the voltage of UOR at 400 mA·cm^{-2} was only 1.47 V (*vs.* RHE). In addition, the electrolytic cell using N-Co_9S_8/Ni_3S_2/NF as cathodes and anodes only shows a low voltage of 1.40 V at the current density of 10 mA·cm^{-2}. In addition to non-metallic element doping, metal ion doping and co-doping methods are also useful. For example, Wang *et al.* prepared a series of M-doped $NiCo_2S_4$/Ni_3S_2 (M = Mn, Fe, Cu, Zn) nanostructures on nickel foam using a one-step hydrothermal method[123]. The introduction of metal ions can not only change the morphology of the catalyst but also provide abundant active sites, thus improving the intrinsic activity of the catalyst. Fe-$NiCo_2S_4$/Ni_3S_2 has the best catalytic activity by comparison. In the electrolyte of 1.0 M KOH and 0.5 M urea, Fe-$NiCo_2S_4$/Ni_3S_2 catalyzed UOR requires only 1.37 and 1.39 V (*vs.* RHE) to achieve current densities of 50 and 100 mA·cm^{-2}, respectively. Figure 10 shows the ball-and-stick model, chemisorption free energy, and calculated state density of water molecules adsorbed on various catalysts, respectively. It can be observed that water molecules have the strongest adsorption energy on the surface of Fe-Co-NiOOH and the highest calculated state density near the Fermi level [Figure 10F]. It shows that Fe-Co-NiOOH plays a key role in water decomposition and has excellent electronic conductivity. The introduction of Fe significantly improves the adsorption performance and conductivity of the catalyst for water and also provides more reactive sites for the catalyst, greatly enhancing the UOR performance.

In another example, Li *et al.* prepared abnormal metastable hcp-CoNi-N/C with metal Co and non-metal N double doping by using a new N-doped induced phase transfer strategy[124]. The catalyst has outstanding UOR performance, and the potential is only 1.31 V at the current density of 10 mA·cm^{-2}. Through experimental analysis and theoretical calculation [Figure 11], it is proved that the electron density of hcp-CoNi-N/C can be controlled by the double doping strategy of metal and non-metal, thus reducing the free energy of urea adsorption on the catalyst surface, facilitating the break of C-N bond, and promoting the electrocatalytic oxidation of urea.

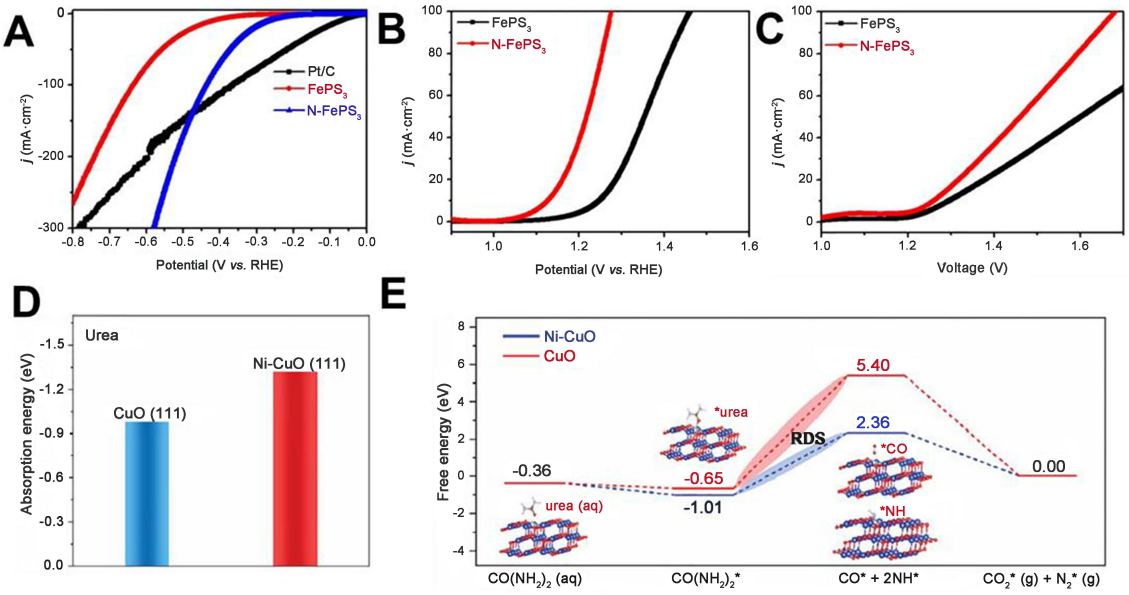

Figure 12. (A) The polarization curves for HER of N-$FePS_3$, $FePS_3$, and Pt/C in 1.0 M KOH; (B) The polarization curves for UOR and the polarization curves for urea electrolysis of N-$FePS_3$ and $FePS_3$ in 1.0 M KOH + 0.33 M glucose; (C) The polarization curves for urea electrolysis of N-$FePS_3$ and $FePS_3$ [23]; (D) The adsorption energy of urea on CuO (111) and Ni-CuO (111); (E) Reaction free spectrum of UOR catalyzed by CuO and Ni-CuO[125]. HER: Hydrogen evolution reaction; UOR: Urea oxidation reaction.

Apart from nickel-based catalysts, other transition metal-based catalysts can also obtain satisfactory UOR properties through rational morphology, structure design, and chemical regulation. For example, Hou *et al.* prepared N_2-doped ferric phosphorus trisulfide nanosheets ($FePS_3$), which showed excellent HER and UOR bi-functional catalytic activities[9]. As shown in Figure 12A, in 1.0 M KOH, the overpotential for HER of N-$FePS_3$ at 200 and 300 mA·cm^{-2} is only 522 and 580 mV, respectively, lower than that of Pt/C. As shown in Figure 12B, in 1.0 M KOH and 0.33 M urea, the UOR of N-$FePS_3$ is only 756 mV at 10 mA·cm^{-2}. When N-$FePS_3$ was used as the cathode and anode to assemble a urea electrolytic cell, as shown in Figure 12C, the cell voltage was 1.26 V when the current density was 10 mA·cm^{-2}, which was about 0.28 V lower than that of the traditional water electrolytic device. Sun *et al.* have grown Ni-doped CuO nanoarrays (Ni-CuO NAs/CF) on 3D copper foam using cation exchange strategies[125]. The catalyst has excellent UOR performance, with a UOR potential of only 1.366 V (*vs.* RHE) at 100 mA·cm^{-2}. Figure 12D shows the comparison of chemisorption energy of urea on CuO (111) and Ni-CuO (111). The lower adsorption energy value indicates that Ni-CuO NAs/CF is more beneficial to the adsorption of urea than CuO NAs/CF, and its intrinsic activity of UOR is stronger. Figure 12E shows the comparison of the free energies of CuO (111) and Ni-CuO (111) surfaces to UOR. Lower free energies also verify the excellent UOR performance of Ni-CuO NAs/CF. The experimental analysis and theoretical calculation showed that nickel doping could effectively enhance the adsorption capacity of urea and enhance its UOR catalytic activity.

Yu *et al.* designed a novel Fe-$Co_{0.85}Se$/FeCo layered double hydroxide (LDH) heterostructure electrocatalyst using a simple *in-situ* selenization method[126]. The catalyst showed excellent bi-functional catalytic performance. UOR and HER only needed 1.48 V and -0.274 V, respectively, to reach a high current density of 500 mA·cm^{-2}. Moreover, the urea-assisted integral electrolysis H_2 production system assembled by the catalyst needs only 1.57 V to reach the current density of 300 mA·cm^{-2}. Finally, the reaction mechanism of UOR and HER was further discussed by *in-situ* Fourier infrared spectroscopy [Figure 13A-C] and DFT [Figure 13D and E]. It was shown that interfacial chemical bonds could regulate the local environment in heterogeneous structures, leading to rapid charge transfer. This optimization of the electron configuration

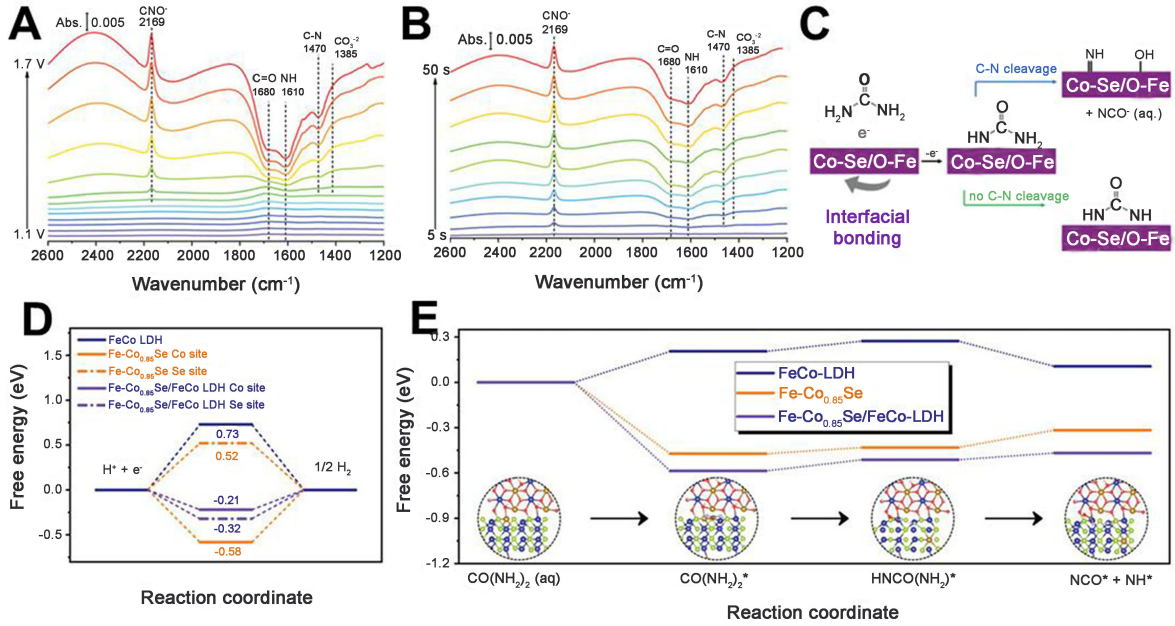

Figure 13. (A) *In-situ* FTIR spectra for Fe-$Co_{0.85}$Se/FeCo LDH in different constant potentials (1.1-1.7 V *vs.* RHE); (B) Under 1.45 V *vs.* RHE, the In-situ time-resolved FTIR measurements of Fe-$Co_{0.85}$Se/FeCo LDH; (C) Diagram of possible intermediates in the critical steps for UOR; (D) Hydrogen adsorption on FeCo LDH, Fe-$Co_{0.85}$Se, and Fe-$Co_{0.85}$Se/FeCo LDH; (E) The diagram of free energy for UOR on FeCo LDH, Fe-$Co_{0.85}$Se, and Fe-$Co_{0.85}$Se/FeCo LDH[126]. LDH: Layered double hydroxide; RHE: reversible hydrogen electrode; UOR: urea oxidation reaction.

promotes the thermodynamic behavior of hydrogen adsorption in HER processes and urea adsorption in UOR processes, effectively improving the catalytic activity of the catalyst.

In recent years, there have been considerable reports on the application of metal organic frame (MOF)-derived materials in UOR. This is because these materials have unique advantages such as adjustable structure, controllable composition, and high porosity, so they have great application potential as efficient electrocatalysts for UOR and HER[127-129]. For example, Zhang *et al.* successfully synthesized a Fe-doped nickel-based MOF nanosheet array catalyst (FeNi-MOF NSs) through the one-step hydrothermal method. In this catalyst, the Fe dopant regulated the electronic structure of MOF[130]. To reach the current density of 10 and 100 mA·cm^{-2}, the overpotentials for UOR of the catalytic were 131 and 155 mV, respectively. The voltage for the electrolytic cell of the dual-electrode system assembled by FeNi-MOF NSs was only 1.431 V at 10 mA·cm^{-2}. Qin *et al.* have grown the nanosheet array structure of oxygen-rich vacancy and vanadium-doped $Ni(OH)_2$ catalyst [O_{vac}-V-$Ni(OH)_2$] on nickel foam, which was used to efficiently oxidize urea to assist H_2 production[66]. The working potential for UOR of O_{vac}-V-$Ni(OH)_2$ is only 1.47 V at 100 mA·cm^{-2}. The good performance of the catalyst is due to the synergistic effect of V doping and oxygen vacancy.

Electrocatalysts for other energy-saving H_2 production systems

Glucose is a widely distributed biomass in nature, which can be converted into gluconic acid, gluconic acid, formic acid, and other compounds with high commercial value. In recent years, due to the advantages of the low theoretical potential of GOR and high added value of products, the H_2 production method of GOR-coupled HER has attracted the attention of researchers. Previously, GOR was generally used in glucose sensors and glucose fuel cells, and a considerable number of GOR materials were precious metal catalysts[131-135]. Precious metal catalysts have excellent catalytic performance and outstanding chemical stability, but their high costs and low reserves have limited their wide application. This has led researchers to explore non-precious metals with affordable prices and abundant reserves, especially the transition

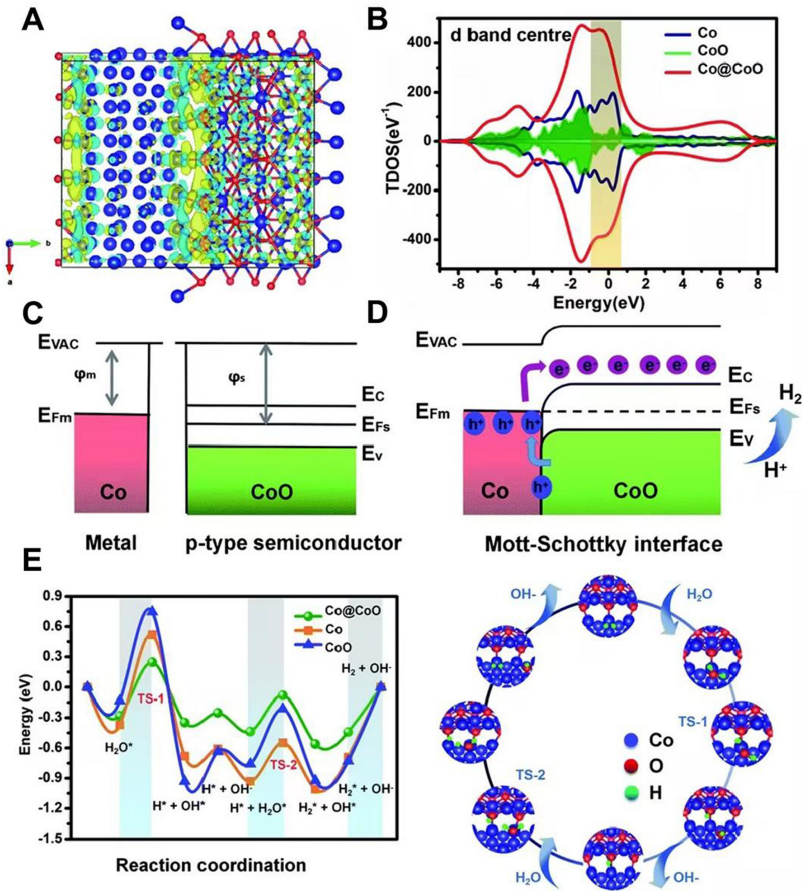

Figure 14. (A) Local charge density difference of the Co@CoO interface. (Yellow and cyan mean electron accumulation and electron depletion, respectively); (B) The calculated state density of Co, CoO, and Co@CoO; Schottky models of semiconductor CoO and metal Co interface (C) before and (D) after contact; (E) Along the reaction coordinate, the relative energy curves of Co, CoO, and Co@CoO and the corresponding Volmer-Heyrovsky process at the Co@CoO interface[136].

metals such as nickel, cobalt, and iron. Recently, cobalt-based catalysts have shown outstanding advantages in the field of GOR. For example, Wu *et al.* used the defect heterogeneity of MOF to prepare core-shell Co@CoO heterojunction[136]. The DFT calculation showed that there was spontaneous electron transfer from Co to CoO during the catalytic process, resulting in the d-band center of the catalyst moving up the Volmer-Heyrovsky path, and the electronic behavior and adsorption/desorption energy of the reaction intermediates were optimized, thus significantly improving the catalytic performance of the catalyst [Figure 14]. At the current density of 20 mA·cm^{-2}, The GOR voltage of Co@CoO is 1.12 V, which is 0.42 V lower than OER. The glucose electrolytic system assembled by Co@CoO only needs 1.34 V to produce 10 mA·cm^{-2}, which is much lower than a water electrolytic system (1.64 V).

In addition, it has been reported that cobalt is used as a dopant to improve the GOR performance. For example, Zhang *et al.* synthesized Co@NCNT by embedding cobalt nanoparticles into N-doped carbon nanotubes, which enables Co@NCNT to have HER, ORR, and GOR multifunctional catalytic performances[137]. For example, Li *et al.* used biomass-based ternary deep eutectic solvent (DES) as a precursor and prepared N_2-doped porous carbon-supported cobalt nanoparticles (Co@NPC)[138]. The catalyst only required a small battery voltage of 1.56 V to provide a current density of 10 mA·cm^{-2}, which was 180 mV lower than the overall water decomposition. Moreover, glucose can be efficiently converted

into lactic acid, formic acid, gluconic acid, and other substances. Another example is Lin *et al*., who designed a cobalt-doped ultra-thin nickel-cobalt hydroxide nanosheet [$Co_{0.5}Ni_{0.5}(OH)_2$ NS] on carbon cloth, whose initial catalytic GOR potential was 1.17 V at the current density of 10 mA·cm^{-2}[139]. The cell voltage is only 1.56 V for glucose oxidation-assisted H_2 production at the current density of 100 mA·cm^{-2}.

Besides cobalt-based catalysts, nickel-based and iron-based catalysts have also been reported as high-performance GOR catalysts. For example, Liu *et al*. recently reported nano-structured NiFe oxide ($NiFeO_x$) and nitride ($NiFeN_x$) catalysts[140]. The two-electrode glucose electrolytic cells with $NiFeO_x$-NF as anodes and $NiFeN_x$-NF as cathodes can provide a high current density of 200 mA·cm^{-2} at 1.48 V and can run stably for 24 h. In addition, 87% and 83% gluconic acid and gluconic acid can be obtained by the reaction of the electrolytic cell. The special feature of this work is that the possible reaction pathways of glucose oxidation are also analyzed by *in-situ* infrared spectroscopy, nuclear magnetic resonance, and other characterization. Du *et al*. prepared a ferric phosphide catalyst (Fe_2P/SSM), which was grown on stainless steel mesh[141]. The cell voltage of a two-electrode glucose electrolytic cell synthesized by this catalyst and Pt/C was 300 mV, lower than that of a cell split by water alone.

In addition, many other small molecule oxidations coupled with HER for H_2 production have also been reported, such as glycerol oxidation (GEOR) and 5-hydroxymethylfurfural oxidation reactions (HMFOR). For example, Xu *et al*. prepared N-doped carbon-coated Ni-Mo-N nanowire arrays on nickel foam substrates (NC/Ni-Mo-N/NF) by hydrothermal methods and calcining processes [Figure 15A][142]. Due to surface modification, electronic structure optimization, and interfacial synergies, NC/Ni-Mo-N/NF showed excellent HER and GEOR properties under alkaline conditions. Li *et al*. reported a nickel-molybdenum nitride nanoplate catalyst (Ni-Mo-N/CFCS) for oxidizing glycerol to formic acid and producing H_2[143]. When it reached 10 mA·cm^{-2}, the GEOR voltage was only 1.30 V, and the voltage of the two-electrode system was only 1.36 V. The Faraday efficiency of formic acid and H_2 was up to 95.0% and 99.7%, respectively. In this work, the authors also demonstrated that formic acid was produced from glycerol using isotopic labeling [Figure 15B]. Zhou *et al*. prepared a Co_4N@CeO_2 heterojunction catalyst. CeO_2 was introduced into the Co_4N system as an "electronic pump" to optimize the internal electronic structure of the catalyst. The Co_4N@CeO_2 showed excellent multifunctional catalytic activities of HER, OER, and HMFOR [Figure 15C][144]. At the current density of 10 mA·cm^{-2}, Co_4N@CeO_2 catalyzes HER and OER as low as 49 and 263 mV in 1.0 M KOH, respectively, and catalyzes HMFOR as low as 1.22 V (*vs*. RHE) in 1.0 M KOH + 0.3 M HMF. In addition, in 1.0 M KOH + 0.3 M HFM, the cell voltage of NF/Co_4N@CeO_2 || NF/Co_4N@CeO_2 two-electrode systems is only 1.33 V to achieve 10 mA·cm^{-2}, which is far lower than that of pure water splitting (1.53 V).

Zhao *et al*. presented the pioneering integration of biomass electroreforming and green H_2 production, where a chitin oxidation reaction (COR) was employed as a substitute for OER in conventional OWS [Figure 16A][145]. The HER process was coupled with chitin electro-oxidation to simultaneously generate H_2 and acetic acid (HAc). Initially, the natural amino biopolymer chitin underwent depolymerization to yield the monomer acetylglucosamine (NAG), which could be further deacetylated to produce HAc and glucosamine. The opening of the pyran ring in glucosamine led to additional HAc formation, resulting in a remarkable overall yield exceeding 90%. Notably, chitin oxidation exhibited superior thermodynamic and kinetic characteristics compared to water oxidation. The main product HAc demonstrated good solubility within the electrolyte and remained stable within the REDOX potential window (-0.4 to 1.7 V *vs*. RHE) with minimal by-product production. Consequently, this integrated approach enabled a reduction in overall energy consumption during electrolysis by approximately 15%.

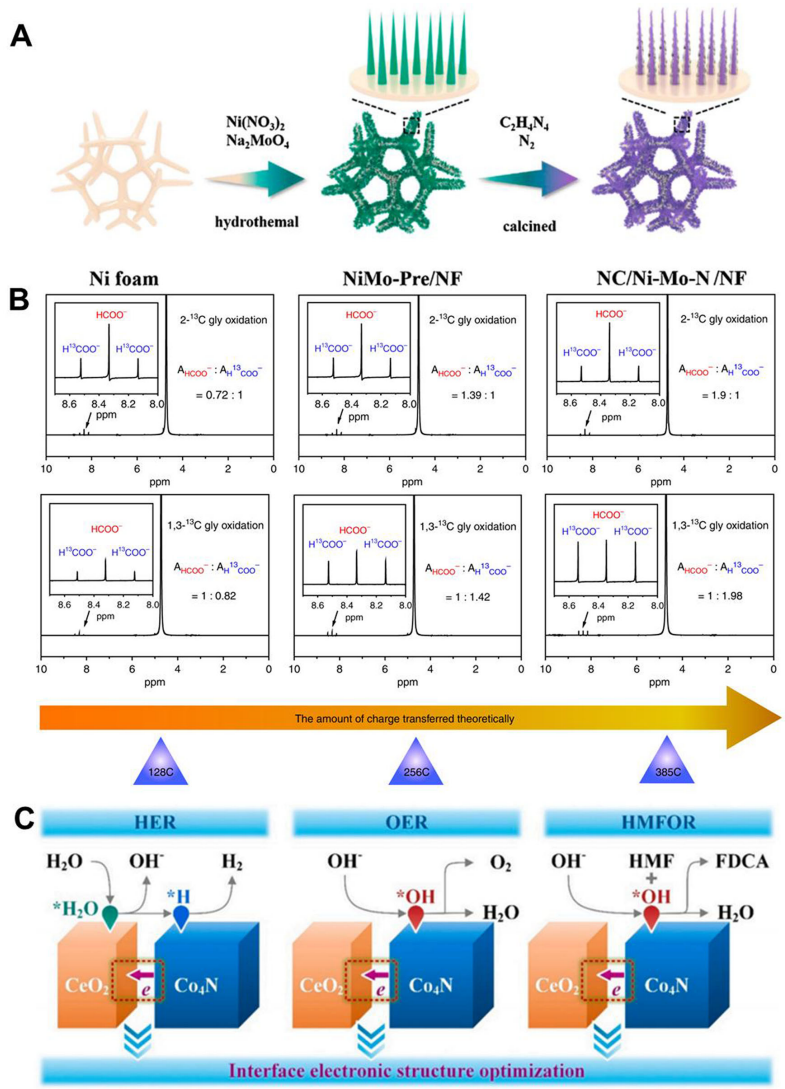

Figure 15. (A) Scheme illustrating the synthesis of the NC/Ni-Mo-N/NF[142]; (B) ^{1}H NMR spectra for the electro-oxidation of 2-^{13}C glycerol and 1, 3-^{13}C glycerol[143]; (C) Schematic diagram of the principle of CeO_2 as "electronic pump" in promoting multifunctional catalytic performances of Co_4N@CeO_2 catalysts[144]. HER: Hydrogen evolution reaction; HMFOR: 5-hydroxymethylfurfural oxidation reaction; NMR: nuclear magnetic resonance; OER: oxygen evolution reaction.

Coal is an abundant and cost-effective source of heavy carbon. The traditional coal gasification to produce H_2 has serious pollution and poor economic benefits. Researchers are endeavoring to establish a coal-assisted electrolytic water H_2 production system. This approach not only enables the clean utilization of coal but also reduces electricity consumption in H_2 production. Coughlin and Farooqu reported the electrocatalytic H_2 production of coal-water systems for the first time[146]. They introduced a coal slurry into the anode solution; the cathode led to H_2, while CO_2 was detected at the anode after a long reaction. Later, the researchers introduced a variety of charge transfer carriers, such as Fe^{2+}/Fe^{3+}, Ce^{4+}/Ce^{3+}, V^{5+}/V^{2+}, Mn^{3+}/Mn^{2+}, $Fe(CN)_6^{3-}/Fe(CN)_6^{4-}$, *etc.* into the system to facilitate the reaction process in the anode region [Figure 16B][147]. These cyclic H_2 productions have higher reaction rates than the conventional coal slurry. The initial current density is more than 100 mA·cm^{-2}. However, the reaction mechanism of electrocatalytic H_2 production in coal-water systems is complicated, and there is still a lack of research and understanding on the evolution law of physical and chemical properties of coal.

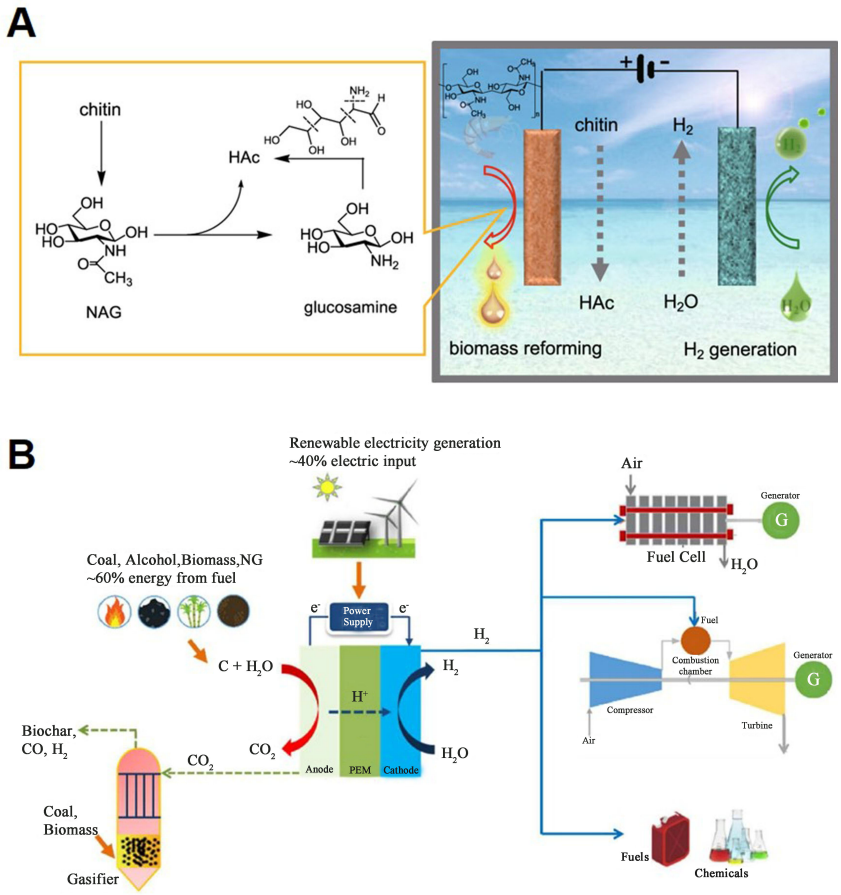

Figure 16. (A) Hybrid electrolysis for raw biomass reforming and hydrogen evolution[145]; (B) Schematic of the carbon-assisted water electrolysis for hydrogen production assembled with renewable energy[147]. NAG: Monomer acetylglucosamine.

Precious metals Pt and Ru and non-precious metals Fe, Co, Ni, and Mo-based materials have been widely investigated in the field of energy-saving reaction-assisted H_2 production, and these systems exhibit cell voltages much lower than the OER-HER couple. Nevertheless, an in-depth understanding of the design principles of electrocatalysts for these reactions, including improving their activity and stability at high current densities and selectivity for specific high value-added products, is urgently needed for practical applications of energy-efficient H_2 generation technologies, but it is rarely achieved.

CONCLUSION

Water electrolysis, as a green H_2 production technology, has gained significant attention in recent decades. However, its high operating voltage has undoubtedly increased the energy consumption of H_2 production. In this review, we reviewed the recent advances in energy-saving anodic reactions to replace OER to reduce the energy consumption of H_2 production, including MOR, HzOR, UOR, GOR, and HMFOR[148-152]. Additionally, these reactions can be used to purify wastewater or to generate high-value-added chemicals simultaneously. Although these reactions possess low equilibrium potentials, they generally involve multi-electron transfer processes with slow kinetics. For example, urea oxidation requires an equilibrium potential of only 0.37 V, much lower than 1.23 V of the OER, yet contains complex six e^- transfer processes to produce N_2 and CO_2. After highlighting the fundamental reaction principles of several typical energy-efficient anodic reaction-assisted H_2 production systems, the preparation methods, regulatory strategies, and composition/structure-performance relations of advanced catalysts for these systems are introduced[153-163]. In addition, the performance of these energy-saving H_2 production systems is summarized in Table 1.

OUTLOOK

Although many high-performance noble and non-noble metal-based catalysts have been developed for these H_2 production systems, several challenges remain in this emerging and fascinating field. First, to reduce the overall operating voltage for H_2 production, the electrocatalysts are expected to have high intrinsic activity for both the anodic and cathodic reactions. However, the anodic reaction (e.g., MOR, UOR, and HzOR) and the HER occurring at the cathode undergo varying catalytic pathways and involve different reaction intermediates (e.g., CH_2O^* and CHO^* for MOR, $N_2H_3^*$ and $N_2H_2^*$ for HzOR) adsorption/desorption at the active sites[164-169]. This poses a great challenge to the design and synthesis of highly active bifunctional catalysts. Modulation of the type, coordination environment, and geometric structure of active sites regulating its energetics with reaction intermediates can enhance intrinsic bifunctional catalytic activity. Strategies for precise atomic-scale regulation of catalysts need to be further developed to meet the needs of practical applications of energy-saving H_2 production technologies. Additionally, factors such as dimensions, morphology, and pore structure also have an important impact on the accessibility of active sites and mass transfer during catalysis, which also need to be taken into account for the design of high-performance catalysts. Consequently, catalyst design and synthesis based on traditional synthetic science requires a great deal of trial and error. Using machine learning (ML) to predict the optimized active site species and coordination environment/geometry combined with high-throughput experimental techniques is expected to improve the efficiency of developing high-performance bifunctional catalysts for energy-saving H_2 production.

Another concern is the surface rearrangement or reconfiguration of catalysts during the catalytic process. For example, transition metal oxides and hydroxides in alkaline electrolytes are sometimes partially converted to (oxy)hydroxides in alkaline electrolytes. Advanced *in-situ* and operando characterization techniques, such as *in situ* ambient-pressure X-ray photoelectron spectroscopy and operando Raman spectra, are highly in demand for investigating the true catalytically active species and exploring the structure-activity relationship. In addition, H_2-producing systems, coupled with other anodic reactions, sometimes produce products that dissolve into the electrolyte. For example, the HMFOR-HER cell may produce 2,5-furandicarboxylic acid, and the GOR-HER cell may produce gluconic acid and arabinose. To enhance the economics and atomic utilization of H_2-producing systems, it is crucial to carefully tune the composition and structure of catalysts to improve the selectivity of specific products. Moreover, improving these energy-saving H_2-producing devices to efficiently separate specific products from the electrolyzer is still a big challenge.

Finally, in order to fully unravel the intricate relationship between the atomic and electronic structures of catalysts and their corresponding catalytic activity in HER electrocatalysts, it is imperative to undertake extensive and meticulous DFT simulations. These simulations offer powerful tools to explore the energetics and kinetics of the reaction, providing invaluable insights into the fundamental mechanisms and reaction pathways involved. However, it is currently uncommon for researchers to consider the solvation effect or pH gradient or both in the DFT model, resulting in simulation outcomes that deviate from actual experimental data. In particular, in some cases, it even contradicts the experimental findings. This discrepancy between theoretical predictions and experimental observations can lead to a lack of consistency and hinder the elucidation of the HER mechanism. To overcome this limitation, it is crucial to enhance the accuracy of DFT simulations by considering the influence of solvation and pH gradients, enabling a more comprehensive understanding of the underlying processes and facilitating the development of robust and reliable theoretical models for HER electrocatalysis. In addition, by examining various catalyst

Table 1. Comparison of the performance of energy-efficient H_2 production systems

	Catalysts	Electrolyte	HER performance	Performance of anodic reactions	Performance of cell	Stability	Ref.
MOAHP	Co-doped Rh	1 M KOH + 1 M CH_3OH 1 M KOH (HER)	E_{10} = 2 mV	889 mA·mg^{-1}	E_{10} = 1.545 V	12 h @ -0.1 V (HER) 14 h @ 1.4 V (device)	[74]
	NMS/CC	1 M KOH + 1 M CH_3OH	E_{10} = 106 mV	E_{100} = 1.38 V	E_{50} = 1.69 V	120 h @ 1.4 V (MOR) 24 h @ 1.8 V (device)	[81]
	PdIn bimetallene	1 KOH + 1 M CH_3OH	E_{10} = 171 mV	2.27 A·mg$^{-1}_{Pd}$	E_{100} = 1.26 V	3,600 s @ -0.2 V (MOR) 15 h @ 10 mA·cm^{-2} (HER) 15 h @ 100 mA·cm^{-2} (device)	[77]
	Pt-CoTe/NC-800	0.5 M H_2SO_4 + 1 M CH_3 OH	E_{10} = 28 mV	/	E_{10} = 0.68 V	22.9 mA·cm^{-2} after 3,600 s (MOR) 30 h @ 10 mA·cm^{-2} (HER) 18 h @ 0.68 V (device)	[55]
	$NiFe_2O_4$/NF	1 M KOH + 0.5 M CH_3 OH	E_{50} = 234 mV	E_{100} = 1.43 V	E_{100} = 1.68 V E_{100} = 1.74 V (seawater)	15 h @ -0.6 V (HER) 7 h @ 2 V (seawater device)	[86]
HOAHP	Ni(Cu)/NF	1.0 M KOH + 0.5 M N_2H_4	/	E_{50} = 204 mV	E_{100} = 0.41 mV	10 h @ 100 mA·cm^{-2} (device)	[39]
	Cu_1Ni_2-N	1.0 M KOH + 0.5 M N_2H_4 (HzOR and device) 1.0 M KOH (HER)	E_{10} = 71.4 mV	E_{10} = 0.5 V	E_{10} = 0.24 V	35 h @ 10 mA·cm^{-2} (HzOR) 70 h @ 10 mA·cm^{-2} (device) 60 h @ 10 mA·cm^{-2} (HER)	[40]
	Rh/NCBs	1.0 M KOH + 0.5 M N_2H_4 (HzOR and device) 1.0 M KOH (HER)	E_{10} = 77 mV	E_{10} = 72 mV	E_{10} = 0.149 V	6,000 s @ 0.03 V (HZOR) 71% after 6,000 s (HER) 6,000 s @ 20 mA·cm^{-2} (device)	[88]
	Ni_3N-Co_3N PNAs/NF	1.0 M KOH + 0.5 M N_2H_4 (HzOR and device) 1.0 M KOH (HER)	E_{10} = -43 mV	E_{10} = -83 mV	E_{10} = 0.071 V	40 h @ -0.105 V (HER) 40 h @ -0.04 V (HzOR) 20 h @ -0.14 V (device)	[58]
	Fe-CoNiP@NC	1 M KOH + 0.5 M N_2H_4 seawater 1 M KOH seawater (HER)	E_{1000} = 0.28 V	E_{1000} = 0.49 V	E_{1000} = 0.56 V	100 h @ 500 mA·cm^{-2} (device)	[102]
UOAHP	N-Co_9S_8/Ni_3S_2 /NF	1 M KOH + 0.5 M urea	E_{10} = 111 mV	E_{10} = 1.37 V	E_{10} = 1.4 V	20 h @ 20 mA·cm^{-2} (HER) 20 h @ 20 mA·cm^{-2} (UOR) 50 h @ 1.77 V (device)	[122]
	N-$FePS_3$	1 M KOH + 0.33 M urea 1 M KOH (HER)	E_{10} = 267 mV	E_{10} = 756 mV	E_{10} = 1.26 V	36 h @ 50 mA·cm^{-2} (device)	[9]
	Fe-$Co_{0.85}$	1 M KOH + 0.5 M urea	E_{500} = 0.274 V	E_{500} = 1.48 V	E_{300} = 1.57 V	50 h @ 10 mA·cm^{-2} (HER)	[126]

	Se/FeCo LDH					60 h @ 10 mA·cm^{-2} (UOR) 60 h @ 100 mA·cm^{-2} (device)	
	FeNi-MOF NSs	1 M KOH + 0.33 M urea	E_{100} = 288 mV	E_{100} = 155 mV	E_{100} = 1.85 V	93.6% after 10 h @ 1.48 V (device)	[130]
	Ovac-V-Ni(OH)$_2$	1 M KOH + 0.33 M urea	/	E_{100} = 1.47 V	E_{10} = 1.5 V	110 h @ 1.37V (UOR)	[66]
Others	Fe_2P/SSM	1 M KOH + 0.5M glucose	/	E_{10} = 1.35 V	E_{10} = 1.22 V	24 h @ 10 mA·cm^{-2} (device)	[141]
	Ni-Mo-N/CFC	1 M KOH + 0.1 M glycerol	E_{10} = 43 mV	E_{10} = 1.3 V	E_{10} = 1.36 V	11 h @ 10 mA·cm^{-2} (device)	[143]
	Co_4N@CeO_2	1 M KOH + 0.3 M HMF	E_{100} = 167 mV	E_{100} = 1.32 V	E_{10} = 1.33 V	/	[144]

CFC: Carbon fiber cloth; FeNi-MOF NSs: Fe-doped nickel-based MOF nanosheet array catalyst; HER: hydrogen evolution reaction; HOAHP: hydrazine oxidation-assisted H_2 production; HzOR: hydrazine oxidation reaction; LDH: layered double hydroxide; MOAHP: methanol oxidation-assisted H_2 production; MOF: metal organic frame; MOR: methanol oxidation reaction; NMS/CC: NiSe/$MoSe_2$ grown on carbon cloth; PNAs/NF: porous nanosheet arrays/nickel foam; NCBs: nitrogen-doped carbon nanobowls; SSM: stainless steel mesh; UOAHP: urea oxidation-assisted H_2 production; UOR: urea oxidation reaction.

compositions, surface configurations, and reaction conditions, the DFT simulations can elucidate the intricate interplay between catalyst structures, surface reactivity, and overall catalytic performance, paving the way for the rational design and optimization of highly efficient and sustainable electrocatalysts for HER electrolysis. Furthermore, we must also establish precise experimental and DFT calculation methods to identify the contributions of other effects (e.g., structural strain and defect engineering) on activity.

DECLARATIONS

Authors' contributions

Prepared and revised the draft: Liu W, Niu X, Tang J, Liu Q, Luo J, Liu X, Zhou Y
All authors contributed to the discussion of the draft.

Availability of data and materials

Not applicable.

Financial support and sponsorship

This work was supported by the Zhejiang Provincial Natural Science Foundation of China (LZ21E020003), the National Natural Science Foundation of China (22275166 and 22075211), and the Zhejiang Province Key Research and Development Project (2023 C01191).

Conflicts of interest

All authors declared that there are no conflicts of interest.

Ethical approval and consent to participate

Not applicable.

Consent for publication

Not applicable.

REFERENCES

1. Liu X, He J, Zhao S, et al. Self-powered H_2 production with bifunctional hydrazine as sole consumable. *Nat Commun* 2018;9:4365. DOI PubMed PMC
2. Peng X, Mi Y, Liu X, et al. Self-driven dual hydrogen production system based on a bifunctional single-atomic Rh catalyst. *J Mater Chem A* 2022;10:6134-45. DOI
3. Palo DR, Dagle RA, Holladay JD. Methanol steam reforming for hydrogen production. *Chem Rev* 2007;107:3992-4021. DOI PubMed
4. Yu H, Li Y, Xu C, Jin F, Ye F, Li X. Distinct facets to enhance the process of hydrogen production via methanol steam reforming - a review. *Energy Stor Sav* 2022;1:53-69. DOI
5. Zhao X, Chen M, Bi Z, Zhang H, Hu G, Zhou Y. Double-confinement construction of atomically-dispersed-Fe bifunctional oxygen electrocatalyst for high-performance zinc-air battery. *Small* ;2023:2304854 (Online ahead of print). DOI PubMed
6. Qin Y, Han X, Li Y, et al. Hollow mesoporous metal-organic frameworks with enhanced diffusion for highly efficient catalysis. *ACS Catal* 2020;10:5973-8. DOI
7. Yu ZY, Duan Y, Feng XY, Yu X, Gao MR, Yu SH. Clean and affordable hydrogen fuel from alkaline water splitting: past, recent progress, and future prospects. *Adv Mater* 2021;33:e2007100. DOI PubMed
8. Liang Z, Guo H, Lei H, Cao R. Co porphyrin-based metal-organic framework for hydrogen evolution reaction and oxygen reduction reaction. *Chin Chem Lett* 2022;33:3999-4002. DOI
9. Hou J, Peng X, Sun J, et al. Accelerating hydrazine-assisted hydrogen production kinetics with Mn dopant modulated CoS_2 nanowire arrays†. *Inorg Chem Front* 2022;9:3047-58. DOI
10. Jia T, Wang L, Zhang L, et al. Engineering vacancy and hydrophobicity of spherical coral-like CuO catalyst for effective electrochemical CO_2 reduction to ethylene. *Surf Interfaces* 2023;38:102841. DOI
11. Hou X, Ding J, Liu W, Zhang S, Luo J, Liu X. Asymmetric coordination environment engineering of atomic catalysts for CO_2 reduction. *Nanomaterials* 2023;13:309. DOI PubMed PMC
12. Jose V, Do V, Prabhu P, et al. Activating amorphous Ru metallenes through Co integration for enhanced water electrolysis. *Adv Energy Mater* 2023;13:2301119. DOI
13. Zhuang S, Tang Y, Tai X, et al. Hydrogen and electricity co-generation from hydrazine-assisted water electrolysis on hierarchical porous heteroatoms-doped CoCu catalysts. *Appl Catal B Environ* 2022;306:121132. DOI
14. Sun P, Zhou Y, Li H, et al. Round-the-clock bifunctional honeycomb-like nitrogen-doped carbon-decorated Co_2P/Mo_2C-heterojunction electrocatalyst for direct water splitting with 18.1% STH efficiency. *Appl Catal B Environ* 2022;310:121354. DOI
15. Wang C, Schechter A, Feng L. Iridium-based catalysts for oxygen evolution reaction in acidic media: mechanism, catalytic promotion effects and recent progress. *Nano Res Energy* 2023;2:e9120056. DOI
16. Zhao X, Zheng M, Zhang Z, et al. Supramolecular Nanosheet evolution into BC_3N matrix improves the hydrogen evolution reaction activity in the pH universality of highly dispersed Pt nanoparticles†. *J Mater Chem A* 2021;9:16427-35. DOI
17. Wang C, Geng Q, Fan L, Li J, Ma L, Li C. Phase engineering oriented defect-rich amorphous/crystalline RuO_2 nanoporous particles for boosting oxygen evolution reaction in acid media. *Nano Res Energy* 2023;2:e9120070. DOI
18. Xu Y, Xue H, Li X, et al. Application of metal-organic frameworks, covalent organic frameworks and their derivates for the metal-air batteries. *Nano Res Energy* 2023;2:e9120052. DOI
19. Zhang H, Qi G, Liu W, et al. Bimetallic phosphoselenide nanosheets as bifunctional catalysts for 5-hydroxymethylfurfural oxidation and hydrogen evolution†. *Inorg Chem Front* 2023;10:2423-9. DOI
20. Yang Q, Liu W, Wang B, et al. Regulating the spatial distribution of metal nanoparticles within metal-organic frameworks to enhance catalytic efficiency. *Nat Commun* 2017;8:14429. DOI PubMed PMC
21. Xu L, Zhang S, Huang L, et al. A novel CoxNi1-xP/fs-Si self-supporting electrodes manufactured via femtosecond laser for highly efficient hydrogen evolution reaction. *Surf Interfaces* 2022;32:102173. DOI
22. Xiang H, Zheng Y, Chen Y, et al. Self-gating enhanced carrier transfer in semiconductor electrocatalyst verified in microdevice. *Chin Chem Lett* 2022;33:3221-6. DOI
23. Zhang H, Qiu Y, Zhang S, Liu Q, Luo J, Liu X. Nitrogen-incorporated iron phosphosulfide nanosheets as efficient bifunctional electrocatalysts for energy-saving hydrogen evolution. *Ionics* 2022;28:3927-34. DOI
24. Qiao N, Yang C, Wang M, Ma X. Two-dimensional TeX(X=C, Si, Ge) monolayers with strong intrinsic electric field for efficiency hydrogen evolution reaction. *Surf Interfaces* 2022;31:102011. DOI
25. Liu B, Chen Z, Xiong R, et al. Enhancing hydrogen evolution reaction performance of transition metal doped two-dimensional electride Ca_2N. *Chin Chem Lett* 2023;34:107643. DOI
26. Do VH, Prabhu P, Jose V, et al. Pd-PdO nanodomains on amorphous Ru metallene oxide for high-performance multifunctional electrocatalysis. *Adv Mater* 2023;35:2208860. DOI PubMed
27. Shan Y, Li T, Liu L. Electronic structure transformation induced by dual-metal orbital hybridization in $Re_xMn_{1-x}S_2$ monolayer for hydrogen evolution reaction. *Surf Interfaces* 2022;28:101671. DOI
28. Liu W, Huang J, Yang Q, et al. Multi-shelled hollow metal-organic frameworks. *Angew Chem Int Ed* 2017;56:5512-6. DOI PubMed
29. Wei T, Liu W, Zhang S, Liu Q, Luo J, Liu X. A dual-functional Bi-doped Co_3O_4 nanosheet array towards high efficiency 5-hydroxymethylfurfural oxidation and hydrogen production†. *Chem Commun* 2023;59:442-5. DOI PubMed
30. Liu W, Niu X, Feng J, et al. Tunable Heterogeneous FeCo alloy-$Mo_{0.82}N$ bifunctional electrocatalysts for temperature-adapted

Zn-air batteries. *ACS Appl Mater Interfaces* 2023;15:15344-52. DOI PubMed

31. Zhang H, Zhao M, Liu H, et al. Ultrastable FeCo bifunctional electrocatalyst on Se-doped CNTs for liquid and flexible all-solid-state rechargeable Zn-air batteries. *Nano Lett* 2021;21:2255-64. DOI PubMed
32. Xu X, Xie J, Liu B, et al. PBA-derived FeCo alloy with core-shell structure embedded in 2D N-doped ultrathin carbon sheets as a bifunctional catalyst for rechargeable Zn-air batteries. *Appl Catal B Environ* 2022;316:121687. DOI
33. Chen J, Huang J, Wang H, et al. Phase-mediated cobalt phosphide with unique core-shell architecture serving as efficient and bifunctional electrocatalyst for hydrogen evolution and oxygen reduction reaction. *Chin Chem Lett* 2022;33:3752-6. DOI
34. Ji Y, Du J, Chen A. Review on heteroatom doping carbonaceous materials toward electrocatalytic carbon dioxide reduction. *Trans Tianjin Univ* 2022;28:292-306. DOI
35. Feng J, Zheng D, Yin R, et al. A wide-temperature adaptive aqueous Zinc-Air battery-based on Cu-Co dual metal-nitrogen-carbon/nanoparticle electrocatalysts. *Small Structures* 2023;4:2200340. DOI
36. Zhao B, Liu J, Xu C, et al. Hollow NiSe nanocrystals heterogenized with carbon nanotubes for efficient electrocatalytic methanol upgrading to boost hydrogen co-production. *Adv Funct Mater* 2021;31:2008812. DOI
37. Liu Y, Hu B, Wu S, et al. Hierarchical nanocomposite electrocatalyst of bimetallic zeolitic imidazolate framework and MoS_2 sheets for non-Pt methanol oxidation and water splitting. *Appl Catal B Environ* 2019;258:117970. DOI
38. Wang T, Cao X, Qin H, Chen X, Li J, Jiao L. Integrating energy-saving hydrogen production with methanol electrooxidation over Mo modified Co_4N nanoarrays†‡. *J Mater Chem A* 2021;9:21094-100. DOI
39. Sun Q, Wang L, Shen Y, et al. Bifunctional copper-doped nickel catalysts enable energy-efficient hydrogen production via hydrazine oxidation and hydrogen evolution reduction. *ACS Sustain Chem Eng* 2018;6:12746-54. DOI
40. Wang Z, Xu L, Huang F, et al. Copper-nickel nitride nanosheets as efficient bifunctional catalysts for hydrazine-assisted electrolytic hydrogen production. *Adv Energy Mater* 2019;9:1900390. DOI
41. Qian Q, Li Y, Liu Y, et al. Hierarchical multi-component nanosheet array electrode with abundant NiCo/$MoNi_4$ heterostructure interfaces enables superior bifunctionality towards hydrazine oxidation assisted energy-saving hydrogen generation. *Chem Eng J* 2021;414:128818. DOI
42. Teng D, Zhang J, Luo X, et al. Remarkably enhanced photodegradation of organic pollutants by NH_2-UiO-66/ZnO composite under visible-light irradiation. *J Renew Mater* 2022;10:2378-91. DOI
43. Kong D, Qi J, Liu D, Zhang X, Pan L, Zou J. Ni-doped $BiVO_4$ with V^{4+} species and oxygen vacancies for efficient photoelectrochemical water splitting. *Trans Tianjin Univ* 2019;25:340-7. DOI
44. Xu Y, Zhang B. Recent advances in electrochemical hydrogen production from water assisted by alternative oxidation reactions. *ChemElectroChem* 2019;6:3214-26. DOI
45. Zhu B, Liang Z, Zou R. Designing advanced catalysts for energy conversion based on urea oxidation reaction. *Small* 2020;16:e1906133. DOI PubMed
46. Li J, Wang S, Sun S, Wu X, Zhang B, Feng L. A review of hetero-structured Ni-based active catalysts for urea electrolysis. *J Mater Chem A* 2022;10:9308-26. DOI
47. Sun H, Xu X, Song Y, Zhou W, Shao Z. Designing high-valence metal sites for electrochemical water splitting. *Adv Funct Mater* 2021;31:2009779. DOI
48. Wang J, Zhang B, Guo W, et al. Toward electrocatalytic methanol oxidation reaction: longstanding debates and emerging catalysts. *Adv Mater* 2023;35:e2211099. DOI
49. Tomaschun G, Dononelli W, Li Y, Bäumer M, Klüner T, Moskaleva LV. Methanol oxidation on the Au(310) surface: a theoretical study. *J Catal* 2018;364:216-27. DOI
50. He D, Cao L, Feng L, et al. Dual modulation of morphology and electronic structures of VN@C electrocatalyst by W doping for boosting hydrogen evolution reaction. *Chin Chem Lett* 2022;33:4781-5. DOI
51. Xiong L, Sun Z, Zhang X, et al. Octahedral gold-silver nanoframes with rich crystalline defects for efficient methanol oxidation manifesting a CO-promoting effect. *Nat Commun* 2019;10:3782. DOI PubMed PMC
52. Zhang Z, Liu J, Wang J, et al. Single-atom catalyst for high-performance methanol oxidation. *Nat Commun* 2021;12:5235. DOI PubMed PMC
53. Tomaschun G, Klüner T. Methanol oxidation on the Pt(321) surface: a theoretical approach on the role of surface morphology and surface coverage effects†. *Phys Chem Chem Phys* 2019;21:18227-39. DOI PubMed
54. Fang Y, Liu Z. First principles Tafel kinetics of methanol oxidation on Pt(111). *Surf Sci* 2015;631:42-7. DOI
55. Zhou Y, Kuang Y, Hu G, Wang X, Feng L. An effective Pt-CoTe/NC catalyst of bifunctional methanol electrolysis for hydrogen generation. *Mater Today Phys* 2022;27:100831. DOI
56. Zeng R, Yang Y, Shen T, et al. Methanol oxidation using ternary ordered intermetallic electrocatalysts: a DEMS study. *ACS Catal* 2020;10:770-6. DOI
57. Li H, Han Y, Zhao H, et al. Fast site-to-site electron transfer of high-entropy alloy nanocatalyst driving redox electrocatalysis. *Nat Commun* 2020;11:5437. DOI PubMed PMC
58. Qian Q, Zhang J, Li J, et al. Artificial heterointerfaces achieve delicate reaction kinetics towards hydrogen evolution and hydrazine oxidation catalysis. *Angew Chem Int Ed* 2021;60:5984-93. DOI
59. Cui T, Chi J, Zhu J, et al. Tuning the size and chemisorption of FeP4 by trace Ru doping for hydrazine-assisted hydrogen evolution in seawater at large-current-density. *Appl Catal B Environ* 2022;319:121950. DOI

60. Ge S, Zhang L, Hou J, et al. Cu_2O-derived PtCu nanoalloy toward energy-efficient hydrogen production via hydrazine electrolysis under large current density. *ACS Appl Energy Mater* 2022;5:9487-94. DOI
61. Jeong Y, Shankar Naik S, Yu Y, et al. Ligand-free monophasic CuPd alloys endow boosted reaction kinetics toward energy-efficient hydrogen fuel production paired with hydrazine oxidation. *J Mater Sci Technol* 2023;143:20-9. DOI
62. Li J, Li Y, Wang J, et al. Elucidating the critical role of ruthenium single atom sites in water dissociation and dehydrogenation behaviors for robust hydrazine oxidation-boosted alkaline hydrogen evolution. *Adv Funct Mater* 2022;32:2109439. DOI
63. Singh RK, Rajavelu K, Montag M, Schechter A. Advances in catalytic electrooxidation of urea: a review. *Energy Tech* 2021;9:2100017. DOI
64. Daramola DA, Singh D, Botte GG. Dissociation rates of urea in the presence of NiOOH catalyst: a DFT analysis. *J Phys Chem A* 2010;114:11513-21. DOI PubMed
65. Xu X, Li J, Zhang C, et al. Controllable transition engineering from homogeneous $NiSe_2$ nanowrinkles to heterogeneous Ni_3Se_4/$NiSe_2$ rod-like nanoarrays for promoted urea-rich water oxidation at large current densities. *Appl Catal B Environ* 2022;319:121949. DOI
66. Qin H, Ye Y, Li J, et al. Synergistic engineering of doping and vacancy in $Ni(OH)_2$ to boost urea electrooxidation. *Adv Funct Mater* 2023;33:2209698. DOI
67. Liu D, Zeng Q, Hu C, et al. Light doping of tungsten into copper-platinum nanoalloys for boosting their electrocatalytic performance in methanol oxidation. *Nano Res Energy* 2022;1:e9120017. DOI
68. Zhang Q, Xia T, Huang H, et al. Autocatalytic reduction-assisted synthesis of segmented porous PtTe nanochains for enhancing methanol oxidation reaction. *Nano Res Energy* 2023;2:e9120041. DOI
69. Zhao X, Zhou Y, Pan D, et al. Tailoring high-index-facet and oxygen defect of black In_2O_{3-x}/In_2O_3 as highly photothermal catalyst for boosting photocatalytic hydrogen evolution and contaminant degradation. *J Environ Chem Eng* 2023;11:109752. DOI
70. Zhang H, Ren W, Guan C, Cheng C. Pt decorated 3D vertical graphene nanosheet arrays for efficient methanol oxidation and hydrogen evolution reactions. *J Mater Chem A* 2017;5:22004-11. DOI
71. Feng Y, Zhao Z, Li F, et al. Highly surface-distorted Pt superstructures for multifunctional electrocatalysis. *Nano Lett* 2021;21:5075-82. DOI
72. Ma G, Zhang X, Zhou G, Wang X. Hydrogen production from methanol reforming electrolysis at NiO nanosheets supported Pt nanoparticles. *Chem Eng J* 2021;411:128292. DOI
73. Li Y, Kidkhunthod P, Zhou Y, Wang X, Lee JM. Dense heterointerfaces and unsaturated coordination synergistically accelerate electrocatalysis in Pt/Pt_5P_2 porous nanocages. *Adv Funct Mater* 2022;32:2205985. DOI
74. Guo Y, Yang X, Liu X, Tong X, Yang N. Coupling methanol oxidation with hydrogen evolution on bifunctional Co-doped rh electrocatalyst for efficient hydrogen generation. *Adv Funct Mater* 2023;33:2209134. DOI
75. Ren W, Zang W, Zhang H, et al. PtCo bimetallic nanoparticles encapsulated in N-doped carbon nanorod arrays for efficient electrocatalysis. *Carbon* 2019;142:206-16. DOI
76. Jiang YC, Sun HY, Li YN, et al. Bifunctional Pd@RhPd core-shell nanodendrites for methanol electrolysis. *ACS Appl Mater Interfaces* 2021;13:35767-76. DOI PubMed
77. Yin S, Liu S, Wang Z, et al. Methanol-assisted energy-saving hydrogen production over defect-rich perforated PdIn bimetallene. *Chem Eng J* 2022;435:134711. DOI
78. Wang H, Cui L, Yin S, et al. Methanol-assisted energy-efficient water splitting over rambutan-like Au@PdRu core-shell nanocatalysts. *J Mater Chem A* 2022;10:18889-94. DOI
79. Sarno M, Ponticorvo E, Scarpa D. PtRh and $PtRh/MoS_2$ nano-electrocatalysts for methanol oxidation and hydrogen evolution reactions. *Chem Eng J* 2019;377:120600. DOI
80. Lu Z, Xie J, Hu J, Wang K, Cao Y. In situ replacement synthesis of Co@NCNT Encapsulated $CoPt_3$@Co_2P heterojunction boosting methanol oxidation and hydrogen evolution. *Small* 2021;17:e2104656. DOI PubMed
81. Peng X, Xie S, Wang X, et al. Energy-saving hydrogen production by the methanol oxidation reaction coupled with the hydrogen evolution reaction co-catalyzed by a phase separation induced heterostructure. *J Mater Chem A* 2022;10:20761-9. DOI
82. Zhao Z, Zhang J, Lei M, Lum Y. Reviewing the impact of halides on electrochemical CO_2 reduction. *Nano Res Energy* 2023;2:e9120044. DOI
83. Liang J, Liu Q, Alshehri AA, Sun X. Recent advances in nanostructured heterogeneous catalysts for N-cycle electrocatalysis. *Nano Res Energy* 2022;1:e9120010. DOI
84. Ahmad T, Liu S, Sajid M, et al. Electrochemical CO_2 reduction to C_{2+} products using Cu-based electrocatalysts: a review. *Nano Res Energy* 2022;1:e9120021. DOI
85. Li K, Fan Q, Chuai H, Liu H, Zhang S, Ma X. Revisiting chlor-alkali electrolyzers: from materials to devices. *Trans Tianjin Univ* 2021;27:202-16. DOI
86. Du X, Tan M, Wei T, et al. Highly efficient and robust nickel-iron bifunctional catalyst coupling selective methanol oxidation and freshwater/seawater hydrogen evolution via CO-free pathway. *Chem Eng J* 2023;452:139404. DOI
87. He L, Liang B, Huang Y, Zhang T. Design strategies of highly selective nickel catalysts for H_2 production via hydrous hydrazine decomposition: a review. *Natl Sci Rev* 2018;5:356-64. DOI
88. Jia N, Liu Y, Wang L, et al. 0.2 V electrolysis voltage-driven alkaline hydrogen production with nitrogen-doped carbon nanobowl-supported ultrafine Rh nanoparticles of 1.4 nm. *ACS Appl Mater Interfaces* 2019;11:35039-49. DOI
89. Zhang C, Liu H, Liu Y, et al. Rh_2S_3/N-doped carbon hybrids as ph-universal bifunctional electrocatalysts for energy-saving hydrogen

evolution. *Small Methods* 2020;4:2000208. DOI

90. Yang Q, Zhu B, Wang F, et al. Ru/NC heterointerfaces boost energy-efficient production of green H_2 over a wide pH range. *Nano Res* 2022;15:5134-42. DOI
91. Yu Y, Lee SJ, Theerthagiri J, Lee Y, Choi MY. Architecting the AuPt alloys for hydrazine oxidation as an anolyte in fuel cell: comparative analysis of hydrazine splitting and water splitting for energy-saving H2 generation. *Appl Catal B Environ* 2022;316:121603. DOI
92. Kuang Y, Feng G, Li P, Bi Y, Li Y, Sun X. Single-crystalline ultrathin nickel nanosheets array from in situ topotactic reduction for active and stable electrocatalysis. *Angew Chem Int Ed Engl* 2016;55:693-7. DOI PubMed PMC
93. Liu Y, Zhang J, Li Y, et al. Manipulating dehydrogenation kinetics through dual-doping Co_3N electrode enables highly efficient hydrazine oxidation assisting self-powered H_2 production. *Nat Commun* 2020;11:1853. DOI PubMed PMC
94. Tang X, Zhang J, Mei B, et al. Synthesis of hollow $CoSe_2$/$MoSe_2$ nanospheres for efficient hydrazine-assisted hydrogen evolution. *Chem Eng J* 2021;404:126529. DOI
95. Zhu Y, Zhang J, Qian Q, et al. Dual nanoislands on Ni/C hybrid nanosheet activate superior hydrazine oxidation-assisted high-efficiency H_2 production. *Angew Chem Int Ed Engl*2022;61:e202113082. DOI PubMed
96. Wei Z, Wang J, Guo S, Tan SC. Towards highly salt-rejecting solar interfacial evaporation: photothermal materials selection, structural designs, and energy management. *Nano Res Energy* 2022;1:e9120014. DOI
97. Zhang L, Liang J, Yue L, et al. Benzoate anions-intercalated NiFe-layered double hydroxide nanosheet array with enhanced stability for electrochemical seawater oxidation. *Nano Res Energy* 2022;1:e9120028. DOI
98. Liu W, Que W, Yin R, et al. Ferrum-molybdenum dual incorporated cobalt oxides as efficient bifunctional anti-corrosion electrocatalyst for seawater splitting. *Appl Catal B Environ* 2023;328:122488. DOI
99. Hussain SN, Men Y, Li Z, Zhao P, Cheng G, Luo W. Molybdenum-induced tuning 3d-orbital electron filling degree of $CoSe_2$ for alkaline hydrogen and oxygen evolution reactions. *Chin Chem Lett* 2023;34:107364. DOI
100. Deng K, Mao Q, Wang W, et al. Defect-rich low-crystalline Rh metallene for efficient chlorine-free H_2 production by hydrazine-assisted seawater splitting. *Appl Catal B Environ* 2022;310:121338. DOI
101. Zhai X, Yu Q, Liu G, et al. Hierarchical microsphere MOF arrays with ultralow Ir doping for efficient hydrogen evolution coupled with hydrazine oxidation in seawater. *J Mater Chem A* 2021;9:27424-33. DOI
102. Wang X, Zhang W, Yu Q, et al. Fe-doped CoNiP@N-doped carbon nanosheet arrays for hydrazine oxidation assisting energy-saving seawater splitting. *Chem Eng J* 2022;446:136987. DOI
103. Guo L, Yu Q, Zhai X, et al. Reduction-induced interface reconstruction to fabricate $MoNi_4$-based hollow nanorods for hydrazine oxidation assisted energy-saving hydrogen production in seawater. *Nano Res* 2022;15:8846-56. DOI
104. Liu Y, Zhang J, Li Y, Qian Q, Li Z, Zhang G. Realizing the synergy of interface engineering and chemical substitution for Ni_3N enables its bifunctionality toward hydrazine oxidation assisted energy-saving hydrogen production. *Adv Funct Mater* 2021;31:2103673. DOI
105. Zhang W, Liu X, Yu Q, et al. In situ electronic redistribution of Ni_2P hierarchical structure for energy-saving hydrogen production in seawater. *Chem Eng J* 2023;454:140210. DOI
106. Wu X, Zhang Z, He C, et al. Mixed-valence cobalt oxides bifunctional electrocatalyst with rich oxygen vacancies for aqueous metal-air batteries. *Chem Eng J* 2023;453:139831. DOI
107. Zheng X, Yang J, Li P, et al. Dual-atom support boosts nickel-catalyzed urea electrooxidation. *Angew Chem Int Ed Engl* 2023;62:e202217449. DOI PubMed
108. Borchers A, Pieler T. Programming pluripotent precursor cells derived from Xenopus embryos to generate specific tissues and organs. *Genes* 2010;1:413-26. DOI PubMed PMC
109. Wu G, Santandreu A, Kellogg W, et al. Carbon nanocomposite catalysts for oxygen reduction and evolution reactions: from nitrogen doping to transition-metal addition. *Nano Energy* 2016;29:83-110. DOI
110. Dong Y, Wu Y, Wang X, et al. Biomimicry-inspired fish scale-like Ni_3N/$FeNi_3N$/NF superhydrophilic/superaerophobic nanoarrays displaying high electrocatalytic performance†. *Nanoscale* 2023;15:1813-23. DOI
111. Zhu X, Dou X, Dai J, et al. Metallic nickel hydroxide nanosheets give superior electrocatalytic oxidation of urea for fuel cells. *Angew Chem Int Ed* 2016;55:12465-9. DOI
112. Qin Z, Liu W, Que W, et al. Non-noble-metal electrocatalysts for oxygen evolution reaction toward seawater splitting: a review. *ChemPhysMater* 2023;2:185-96. DOI
113. Ding J, Yang H, Zhang S, et al. Advances in the electrocatalytic hydrogen evolution reaction by metal nanoclusters-based materials. *Small* 2022;18:2204524. DOI PubMed
114. Liu W, Zheng D, Zhang L, et al. Bioinspired interfacial engineering of a $CoSe_2$ decorated carbon framework cathode towards temperature-tolerant and flexible Zn-air batteries†. *Nanoscale* 2021;13:3019-26. DOI
115. Hu S, Feng C, Wang S, et al. Ni_3N/NF as bifunctional catalysts for both hydrogen generation and urea decomposition. *ACS Appl Mater Interfaces* 2019;11:13168-75. DOI PubMed
116. Liu W, Que W, Shen X, et al. Unlocking active metal site of Ti-MOF for boosted heterogeneous catalysis via a facile coordinative reconstruction. *Nanotechnology* 2021;33:025401. DOI
117. Gao S, Wei T, Sun J, et al. Atomically dispersed metal-based catalysts for Zn-CO_2 batteries. *Small Structures* 2022;3:2200086. DOI
118. Sha L, Yin J, Ye K, et al. The construction of self-supported thorny leaf-like nickel-cobalt bimetal phosphides as efficient

bifunctional electrocatalysts for urea electrolysis. *J Mater Chem A* 2019;7:9078-85. DOI

119. Wang X, Wang J, Sun X, et al. Hierarchical coral-like NiMoS nanohybrids as highly efficient bifunctional electrocatalysts for overall urea electrolysis. *Nano Res* 2018;11:988-96. DOI
120. Peng Y, Tan Q, Huang H, et al. Customization of functional MOFs by a modular design strategy for target applications. *Chem Synth* 2022;2:15. DOI
121. Yu X, Yu Z, Zhao H, Gates ID, Hu J. Photothermal catalytic H_2 production over hierarchical porous $CaTiO_3$ with plasmonic gold nanoparticles. *Chem Synth* 2023;3:3. DOI
122. Xie H, Feng Y, He X, et al. Construction of nitrogen-doped biphasic transition-metal sulfide nanosheet electrode for energy-efficient hydrogen production via urea electrolysis. *Small* 2023;19:2207425. DOI
123. Wang Y, Chen N, Du X, Han X, Zhang X. Transition metal atoms M (M = Mn, Fe, Cu, Zn) doped nickel-cobalt sulfides on the Ni foam for efficient oxygen evolution reaction and urea oxidation reaction. *J Alloys Compd* 2022;893:162269. DOI
124. Li P, Huang Y, Ouyang X, Li W, Li F, Tian S. Unusual hcp Ni with metal and non-metal dual doping modulation to realize boosted urea oxidation. *Chem Eng J* 2023;464:142570. DOI
125. Sun H, Liu J, Kim H, et al. Ni-doped CuO nanoarrays activate urea adsorption and stabilizes reaction intermediates to achieve high-performance urea oxidation catalysts. *Adv Sci* 2022;9:2204800. DOI PubMed PMC
126. Yu H, Zhu S, Hao Y, et al. Modulating local interfacial bonding environment of heterostructures for energy-saving hydrogen production at high current densities. *Adv Funct Mater* 2023;33:2212811. DOI
127. Liu W, Feng J, Yin R, et al. Tailoring oxygenated groups of monolithic cobalt-nitrogen-carbon frameworks for highly efficient hydrogen peroxide production in acidic media. *Chem Eng J* 2022;430:132990. DOI
128. Gao S, Wang T, Jin M, et al. Bifunctional Nb-N-C atomic catalyst for aqueous Zn-air battery driving CO_2 electrolysis. *Sci Chin Mater* 2023;66:1013-23. DOI
129. Zhang S, Fu J, Xing G, Zhu W, Ben T. Recent advances in porous adsorbent assisted atmospheric water harvesting: a review of adsorbent materials. *Chem Synth* 2023;3:10. DOI
130. Zhang X, Fang X, Zhu K, et al. Fe-doping induced electronic structure reconstruction in Ni-based metal-organic framework for improved energy-saving hydrogen production via urea degradation. *J Power Sources* 2022;520:230882. DOI
131. Xie S, Zhai T, Li W, et al. Hydrogen production from solar driven glucose oxidation over $Ni(OH)_2$ functionalized electroreduced-TiO_2 nanowire arrays†. *Green Chem* 2013;15:2434-40. DOI
132. Liu L, Ci S, Bi L, Jia J, Wen Z. Three-dimensional nanoarchitectures of Co nanoparticles inlayed on N-doped macroporous carbon as bifunctional electrocatalysts for glucose fuel cells. *J Mater Chem A* 2017;5:14763-74. DOI
133. Xu H, Ci S, Ding Y, Wang G, Wen Z. Recent advances in precious metal-free bifunctional catalysts for electrochemical conversion systems. *J Mater Chem A* 2019;7:8006-29. DOI
134. Zheng D, Li J, Ci S, et al. Three-birds-with-one-stone electrolysis for energy-efficiency production of gluconate and hydrogen. *Appl Catal B Environ* 2020;277:119178. DOI
135. Liu W, Feng J, Wei T, et al. Active-site and interface engineering of cathode materials for aqueous Zn-gas batteries. *Nano Res* 2023;16:2325-46. DOI
136. Wu M, Zhao J, Li C, Liu R. Heterogeneity in a metal-organic framework *in situ* guides engineering Co@CoO heterojunction for electrocatalytic H_2 production in tandem with glucose oxidation†. *J Mater Chem A* 2022;10:4791-9. DOI
137. Zhang E, Xie Y, Ci S, et al. Multifunctional high-activity and robust electrocatalyst derived from metal-organic frameworks. *J Mater Chem A* 2016;4:17288-98. DOI
138. Li D, Huang Y, Li Z, Zhong L, Liu C, Peng X. Deep eutectic solvents derived carbon-based efficient electrocatalyst for boosting H_2 production coupled with glucose oxidation. *Chem Eng J* 2022;430:132783. DOI
139. Lin C, Li H, Zhang P, et al. Boosting water electrolysis with anodic glucose oxidation reaction over engineered cobalt nickel hydroxide nanosheet on carbon cloth. *J Electroanal Chem* 2020;861:113946. DOI
140. Liu WJ, Xu Z, Zhao D, et al. Efficient electrochemical production of glucaric acid and H_2 via glucose electrolysis. *Nat Commun* 2020;11:265. DOI PubMed PMC
141. Du P, Zhang J, Liu Y, Huang M. Hydrogen generation from catalytic glucose oxidation by Fe-based electrocatalysts. *Electrochem Commun* 2017;83:11-5. DOI
142. Xu Y, Liu M, Wang S, et al. Integrating electrocatalytic hydrogen generation with selective oxidation of glycerol to formate over bifunctional nitrogen-doped carbon coated nickel-molybdenum-nitrogen nanowire arrays. *Appl Catal B Environ* 2021;298:120493. DOI
143. Li Y, Wei X, Chen L, Shi J, He M. Nickel-molybdenum nitride nanoplate electrocatalysts for concurrent electrolytic hydrogen and formate productions. *Nat Commun* 2019;10:5335. DOI PubMed PMC
144. Zhou P, Hai G, Zhao G, et al. CeO_2 as an "electron pump" to boost the performance of Co_4N in electrocatalytic hydrogen evolution, oxygen evolution and biomass oxidation valorization. *Appl Catal B Environ* 2023;325:122364. DOI
145. Zhao H, Lu D, Wang J, et al. Raw biomass electroreforming coupled to green hydrogen generation. *Nat Commun* 2021;12:2008. DOI PubMed PMC
146. Coughlin RW, Farooque M. Hydrogen production from coal, water and electrons. *Nature* 1979;279:301-3. DOI
147. Ying Z, Geng Z, Zheng X, Dou B, Cui G. Improving water electrolysis assisted by anodic biochar oxidation for clean hydrogen production. *Energy* 2022;238:121793. DOI

148. Fan H, Yu H, Zhang Y, et al. Fe-doped Ni_3C nanodots in N-doped carbon nanosheets for efficient hydrogen-evolution and oxygen-evolution electrocatalysis. *Angew Chem Int Ed Engl* 2017;56:12566-70. DOI PubMed
149. Zhang J, Huang S, Ning P, et al. Nested hollow architectures of nitrogen-doped carbon-decorated Fe, Co, Ni-based phosphides for boosting water and urea electrolysis. *Nano Res* 2022;15:1916-25. DOI
150. Xu X, Hou X, Du P, et al. Controllable Ni/NiO interface engineering on N-doped carbon spheres for boosted alkaline water-to-hydrogen conversion by urea electrolysis. *Nano Res* 2022;15:7124-33. DOI
151. Ang H, Wang H, Li B, Zong Y, Wang X, Yan Q. 3D hierarchical porous Mo_2C for efficient hydrogen evolution. *Small* 2016;12:2859-65. DOI
152. Liu W, Dai X, Guo W, et al. Phase engineering of molybdenum carbide-cobalt heterostructures for long-lasting Zn-Air batteries. *ACS Appl Mater Interfaces* 2023;15:41476-82. DOI
153. Zhang C, Guo Z, Tian Y, Yu C, Liu K, Jiang L. Engineering electrode wettability to enhance mass transfer in hydrogen evolution reaction. *Nano Res Energy* 2023;2:e9120063. DOI
154. Chen J, Abazari R, Adegoke KA, et al. Metal-organic frameworks and derived materials as photocatalysts for water splitting and carbon dioxide reduction. *Coord Chem Rev* 2022;469:214664. DOI
155. Chen S, Lian K, Liu W, et al. Engineering active sites of cathodic materials for high-performance Zn-nitrogen batteries. *Nano Res* 2023;16:9214-30. DOI
156. Zhang H, Wei T, Qiu Y, et al. Recent progress in metal phosphorous chalcogenides: potential high-performance electrocatalysts. *Small* 2023;19:e2207249. DOI PubMed
157. Zhang W, Qin X, Wei T, Liu Q, Luo J, Liu X. Single atomic cerium sites anchored on nitrogen-doped hollow carbon spheres for highly selective electroreduction of nitric oxide to ammonia. *J Colloid Interface Sci* 2023;638:650-7. DOI
158. Qi D, Lv F, Wei T, et al. High-efficiency electrocatalytic NO reduction to NH_3 by nanoporous VN. *Nano Res Energy* 2022;1:e9120022. DOI
159. Theerthagiri J, Karuppasamy K, Lee SJ, et al. Fundamentals and comprehensive insights on pulsed laser synthesis of advanced materials for diverse photo- and electrocatalytic applications. *Light Sci Appl* 2022;11:250. DOI PubMed PMC
160. Wu T, Sun M, Huang B. Non-noble metal-based bifunctional electrocatalysts for hydrogen production. *Rare Met* 2022;41:2169-83. DOI
161. Zhang Z, Liu G, Cui X, et al. Crystal phase and architecture engineering of lotus-thalamus-shaped Pt-Ni anisotropic superstructures for highly efficient electrochemical hydrogen evolution. *Adv Mater* 2018;30:1801741. DOI
162. Guo X, Guo S, Wu C, Li J, Liu C, Chen W. Intelligent monitoring for safety-enhanced lithium-ion/sodium-ion batteries. *Adv Energy Mater* 2023;13:2203903. DOI
163. Lee SJ, Theerthagiri J, Nithyadharseni P, et al. Heteroatom-doped graphene-based materials for sustainable energy applications: a review. *Renew Sustain Energy Rev* 2021;143:110849. DOI
164. Zhang Q, Lian K, Liu Q, et al. High entropy alloy nanoparticles as efficient catalysts for alkaline overall seawater splitting and Zn-air batteries. *J Colloid Interface Sci* 2023;646:844-54. DOI
165. Wei T, Meng G, Zhou Y, et al. Amorphous Fe-Co oxide as an active and durable bifunctional catalyst for the urea-assisted H_2 evolution reaction in seawater†. *Chem Commun* 2023;59:9992-5. DOI
166. Hao P, Dong X, Wen H, et al. *In-situ* assembly of 2D/3D porous nickel cobalt sulfide solid solution as superior pre-catalysts to boost multi-functional electrocatalytic oxidation. *Chin Chem Lett* 2023;34:107843. DOI
167. Fan Z, Luo Z, Huang X, et al. Synthesis of 4H/fcc noble multimetallic nanoribbons for electrocatalytic hydrogen evolution reaction. *J Am Chem Soc* 2016;138:1414-9. DOI
168. Hu W, Zheng M, Duan H, et al. Heat treatment-induced Co^{3+} enrichment in CoFePBA to enhance OER electrocatalytic performance. *Chin Chem Lett* 2022;33:1412-6. DOI
169. Wang T, Gao S, Wei T, et al. Co nanoparticles confined in mesoporous Mo/N Co-doped polyhedral carbon frameworks towards high-efficiency oxygen reduction. *Chemistry* 2023;29:e202204034. DOI PubMed